

# A Non-Phantom Alternative to Phantom Dark Energy in DESI DR2

Cody Hudock<sup>a</sup>

<sup>a</sup>Information Physics Institute, Gosport, Hampshire, UK

## ABSTRACT

The DESI DR2 baryon acoustic oscillation measurements, combined with Planck CMB priors, prefer  $w_0w_a$ CDM over  $\Lambda$ CDM with the best-fit point in the phantom regime ( $w < -1$ )—a trajectory with no healthy field-theoretic realization. We show that a one-parameter Interacting Dark Energy (IDE) model with coupling  $\Gamma(z) = 3A H(z) \Omega_m(z) \Omega_{DE}(z)$  accommodates the DESI signal without phantom crossing, and is BIC-preferred over four-parameter  $w_0w_a$ CDM in every one of four dataset combinations tested: BAO+CMB, BAO+CMB+Pantheon+, BAO+CMB+RSD, and the full BAO+CMB+Pantheon++RSD joint fit. The total  $\Delta$ BIC vs CPL runs from +1.45 on BAO+CMB to +5.74 on the full joint fit. The interpretation is a parsimony statement, not a fit-quality one: in three of four combinations CPL achieves slightly better raw  $\chi^2$ , but its three extra parameters fail the canonical BIC criterion that an extension must reduce  $\chi^2$  by more than  $\ln N$ . The fitted coupling amplitude  $|A|$  is stable at 0.021–0.026 across all four combinations—a  $\sim 25\%$  spread well inside the profile-likelihood uncertainty of any single fit. The most physically informative single result is the BAO+CMB+RSD combination, where IDE is preferred over  $\Lambda$ CDM at  $2.52\sigma$  from directly integrated coupled growth, with the same coupling amplitude appearing in a structurally separate physical sector from the BAO expansion-history measurements that produced the original DESI anomaly. In Pantheon+-inclusive combinations, both extensions are BIC-disfavored relative to  $\Lambda$ CDM due to the well-known DESI-vs-Pantheon+ data tension; the BIC preference for IDE over CPL between the two extensions is robust across all four combinations. Coupled linear perturbation theory yields  $S_8 \approx 0.799$ , directionally closing roughly half of the approximate Planck–weak-lensing tension; the weak-lensing values themselves assume  $\Lambda$ CDM, so this comparison is pending native IDE reanalysis of the shear data. The substrate framework that motivates the coupling form predicts  $|A|$  of order  $\sim 10^{-1.5}$ ; the fitted value is consistent with this expectation but does not test any specific information bound. The model-comparison result can be read as pure phenomenology, independent of the substrate motivation.

## 1. Introduction

The DESI DR2 baryon acoustic oscillation release [1], taken together with Planck CMB priors, prefers the  $w_0w_a$ CDM parametrization over  $\Lambda$ CDM at roughly  $3\sigma$  on expansion-history observables. The best-fit point pushes the dark-energy equation of state into the phantom regime ( $w < -1$ ) over an intermediate redshift band, producing the bell-shaped excursion

$$\rho_{DE}(z) = \rho_{DE,0} a^{-3(1+w_0+w_a)} \exp[-3w_a(1-a)], \quad (1)$$

which peaks near  $z \simeq 0.3$ – $0.5$  before declining at higher redshift.

This is awkward physics. A single canonical scalar field cannot cross  $w = -1$  without violating the null energy condition [2, 3], and multi-field, non-canonical, or higher-derivative constructions intended to evade that constraint generically introduce ghost instabilities or superluminal propagation [4]. The DESI signal is therefore usually read in one of two ways: as a statistical artifact of dataset tensions [5, 6, 7], or as evidence for new physics outside standard scalar-field dark energy.

There is a third reading, and it is the one we develop here. If the dark sector is actually interacting [8, 9], the data are being processed through a wrong template. With an

exchange term  $Q$  coupling the two continuity equations,

$$\dot{\rho}_{DM} + 3H\rho_{DM} = -Q, \quad (2)$$


$$\dot{\rho}_{DE} + 3H(1+w_{\text{bare}})\rho_{DE} = +Q, \quad (3)$$

an analyst who assumes  $Q = 0$  and fits the data with a non-interacting CPL template will infer

$$w_{\text{eff}}(z) = w_{\text{bare}} - \frac{Q(z)}{3H\rho_{DE}}, \quad (4)$$

which can be driven above or below  $-1$  by the sign of  $Q$  even though  $w_{\text{bare}}$  never crosses the divide. This “apparent- $w$  from interacting dark sector” identification is well-known in the IDE literature [45, 46] and is implicit in many subsequent analyses; we reproduce it here as a starting point rather than as a novel observation. With  $Q > 0$  (capacity flowing from dark matter into dark energy) the inferred  $w_{\text{eff}}$  sits below  $-1$ ; with  $Q < 0$  it sits above. As we will see, the data prefer the  $Q < 0$  regime, putting the best-fit interaction firmly in the quintessence-like, non-phantom range.

Equation (4) carries both a theoretical and an empirical message. The theoretical message is that a phantom signature in a CPL fit is not, by itself, evidence of phantom physics. The empirical message is that the DESI data cannot distinguish genuine phantom CPL from a templated CPL fit reading off an underlying interaction. We develop the second case using a bilinear coupling  $\Gamma \propto H \Omega_m \Omega_{DE}$  derived in Sec. 2, and we show that the resulting model fits the data at

 cody.hudock@informationphysicsinstitute.net (C. Hudock)  
ORCID(s):

parity with CPL while staying everywhere within standard energy conditions.

The headline result is a model-comparison statement. Across four dataset combinations—BAO+CMB, BAO+CMB+Pantheon+, BAO+CMB+RSD, and the full BAO+CMB+Pantheon++RSD joint fit—the bilinear IDE model is BIC-preferred over  $w_0w_a$ CDM in every case, with the total  $\Delta\text{BIC}$  vs CPL rising from +1.45 on BAO+CMB to +5.74 on the full joint fit. We report the decomposition of this preference explicitly in Table 2: in three of four combinations CPL achieves slightly better raw  $\chi^2$  than IDE, but fails to earn its extra parameter’s  $\ln N$  penalty. The BIC preference for IDE is therefore a parsimony statement—CPL’s additional free parameter does not reduce  $\chi^2$  by more than  $\ln N$ —rather than a claim that IDE fits the data better in raw  $\chi^2$ . The rise in total  $\Delta\text{BIC}$  with dataset size reflects the  $\ln N$  penalty growing, not the data preferring IDE more strongly. We note a further caveat: on the two SN-inclusive fits, both extended models are disfavored relative to  $\Lambda$ CDM due to the well-known DESI-vs-Pantheon+ tension [5, 7]. The comparison reported here is between the two extensions; the separate question of whether either extension is preferred over  $\Lambda$ CDM depends on how one weighs the DESI and Pantheon+ data against each other, and is a property of the data rather than of either dark-energy model.

The fitted coupling amplitude  $|A|$  stays at 0.021–0.026 across all four combinations, a  $\sim 25\%$  spread that fits comfortably within the profile-likelihood uncertainty of any single fit (Sec. 4.3). That stability matters: if the IDE signal were really an artifact of the DESI-vs-Pantheon+ tension, different dataset combinations would push  $A$  to noticeably different values, and they don’t.

The redshift-space distortion (RSD) data confirm this from a different direction. On BAO+CMB+RSD alone, with no supernovae included anywhere in the fit, IDE is preferred over  $\Lambda$ CDM at  $\Delta\chi^2 = 6.33$  corresponding to  $2.52\sigma$  for a single extra parameter, computed from the directly integrated coupled growth equations. We note that the RSD fit still uses the BAO+CMB data for the background expansion, so “independent” here means independent physical sector (growth of structure vs. expansion history), not independent measurement: the BAO and RSD constraints share the same underlying BAO scale calibration. With only 22 data points total in this combination, the BIC-level statement ( $\Delta\text{BIC} = +3.24$  vs  $\Lambda$ CDM, +4.15 vs CPL) is suggestive rather than definitive—the small- $N$  asymptotic approximation BIC relies on is less well-justified at this sample size. What we can state robustly is that the growth and expansion sectors are not pointing in opposite directions at the coupling amplitude.

Coupled linear perturbation theory at the best-fit interaction, using lattice-frame boundary conditions appropriate to a substrate-based dark energy (Sec. 5.6), yields  $S_8 \approx 0.799$  in the sub-horizon quasi-static limit—a 3.9% reduction from the Planck- $\Lambda$ CDM extrapolation of 0.831. We emphasize immediately that the weak-lensing  $S_8$  measurements used as comparison here themselves assume  $\Lambda$ CDM in their shear-to-power-spectrum pipeline, so this comparison should be

read as a direction-and-magnitude check rather than a precision tension assessment; a fully consistent analysis requires refitting the KiDS and DES shear data with the IDE model in the forward pipeline. With that caveat in place, the  $S_8$  prediction directionally closes roughly half of the Planck-vs-weak-lensing tension, dropping it from roughly  $3.1\sigma$  to  $1.5\sigma$  in the approximate comparison.

The bilinear coupling form

$$\Gamma(z) = 3A \cdot H(z) \Omega_m(z) \Omega_{\text{DE}}(z), \quad (5)$$

is derived in Sec. 2 from two independent physical arguments: Gibbons–Hawking Landauer kinetics at the cosmological horizon, which sets the Hubble scaling, and mean-field bimolecular transition statistics, which sets the bilinear  $\Omega_m \Omega_{\text{DE}}$  population factor. The substrate framework predicts  $|A|$  of order  $\sim 10^{-1.5}$ , with the specific value depending on which information bound saturates and on a geometric prefactor  $C$  we do not derive from first principles. The empirical fit gives a best-fit  $|A| = 0.021$  with an asymmetric profile-likelihood interval of approximately  $[0.010, 0.033]$  (Sec. 4.3). The fitted value is consistent with this order-of-magnitude expectation but does not independently test any specific information bound; given the factor-of-two theoretical uncertainty across different bound choices and the factor-of-three empirical uncertainty in  $|A|$ , the consistency check is meaningful as a sanity check but should not be read as a precision validation of horizon-scale Landauer physics. See Sec. 2.3 for a careful statement of what the prediction does and does not claim.

The model-comparison claim does not require any commitment to the substrate framework. A reader who is unmoved by the derivation can read this paper as pure phenomenology: the bilinear form  $\Gamma \propto H \Omega_m \Omega_{\text{DE}}$  accommodates the DESI anomaly without phantom crossing and is BIC-favored over CPL. The substrate-physics motivation in Sec. 2 explains why this particular form rather than some arbitrary alternative, but its plausibility and the question of whether the coupling fits the data are separate.

One technical point about the scope of the fit: current data are agnostic to the bare dark-energy equation of state across the range  $w_{\text{bare}} \in [-1, -0.96]$ . The interaction amplitude  $A$  does the heavy lifting in accommodating the DESI signal, and the  $w_{\text{bare}}-A$  degeneracy is unbroken at present precision (Sec. 5.5). This is a feature rather than a bug: the data select the interacting interpretation at the level of  $w_{\text{eff}}(z)$ , independently of which specific mechanism sources the bare equation of state.

The paper proceeds as follows. Section 2 develops the substrate derivation of  $\Gamma(z)$ . Section 3 describes the data and likelihood. Section 4 reports the fits and parameter uncertainties across all four dataset combinations. Section 5 works through the physical interpretation, the BIC framing, the  $w_{\text{bare}}$  degeneracy, the  $S_8$  calculation, and the predictions that future data will test. Section 6 summarizes.

## 2. Theoretical Framework

We consider an interacting dark energy model with coupling

$$\Gamma(z) = 3A \cdot H(z) \Omega_m(z) \Omega_{\text{DE}}(z).$$

This functional form emerges from physics arguments developed below; a reader who declines those arguments can treat it as a physics-motivated phenomenological prior, and the empirical question of whether the coupling fits the data is settled directly by the fits of Sec. 4. The derivation situates the coupling within the Symbiotic Infodynamic Equilibrium (SIE) framework [15]. The Landauer-kinetic derivation in Sec. 2.3 rests on established foundations: the Bekenstein area-entropy bound [35], Landauer's thermodynamic cost of computation [17], the holographic principle [36, 37], and Jacobson's thermodynamic derivation of Einstein's equations [38]. Verlinde's entropic-gravity program [39] and Vopson's mass-energy-information equivalence [40, 18] are noted as framework context but not invoked in the derivation itself.

### 2.1. The SIE Dark Sector

Within SIE, the macroscopic vacuum is modeled as a discrete computational substrate operating at the Bekenstein holographic saturation limit, with gravitational, dark-matter, and dark-energy phenomena emerging from the substrate's information-processing constraints rather than entering as independent primitives. The framework is developed in Ref. [15], currently a Zenodo preprint rather than a peer-reviewed publication. We flag this explicitly so readers can calibrate the framework's external validation status; the present paper's empirical content and model-comparison results are independent of that external validation, as discussed in Sec. 2 opener. Each Planck-scale node occupies one of two dynamical states: a *matter-processing* node carries localized rest-mass or radiation degrees of freedom; an *idle* node maintains spatial coherence by paying the Landauer erasure cost of its stored information [17, 18].

Dark matter, in this picture, is the lattice's restorative response to macroscopic defect translation: baryonic mass aggregates drag the surrounding substrate, and the resulting infodynamic viscosity contributes an effective dust-like density  $\rho_{\text{DM}} \propto a^{-3}$ , dressed by the interaction term we are about to develop.

Dark energy is the Landauer erasure cost of the idle-node population. The SIE identification

$$\rho_{\text{DE}}(z) = \phi(z) \rho_{\text{crit}}(z), \quad \phi(z) \equiv \Omega_{\text{DE}}(z), \quad (6)$$

recovers  $\rho_{\text{DE}} \rightarrow \text{const}$  in the de Sitter limit  $\phi \rightarrow 1$  and vanishes as  $\phi \rightarrow 0$  during matter domination. The bare equation of state of this idle-node Landauer energy is naturally  $w_{\text{bare}} = -1$ , which we adopt as the baseline. A mild departure  $w_{\text{bare}} \approx -0.96$  is also compatible with the framework at the isotope-decay slow-roll level, and current data do not distinguish the two values at present precision (Sec. 5.5).

### 2.2. Interaction from Strain-Capacity Balance

The two sectors share a common conserved substrate: every idle node is one not supporting a matter-processing mode, and vice versa. Capacity released or absorbed during substrate state transitions therefore flows between the two sectors, captured by Eqs. (2)–(3) with  $Q$  the volumetric transfer rate. The bare EOS of the Landauer idle-node energy density is  $w_{\text{bare}} = -1$  exactly; the idle contribution evolves only through the  $Q$  term. The functional form of  $\Gamma \equiv Q/\rho_{\text{DE}}$  is derived next from two independent substrate-physics arguments.

*Covariant energy-momentum transfer convention.* In a fully covariant treatment the exchange is described by a four-vector  $Q^\mu$  appearing on the right-hand side of  $\nabla_\nu T^{\mu\nu} = Q^\mu$ , with  $\sum_i Q^\mu_{(i)} = 0$  enforcing overall conservation. A standard IDE convention fixes the direction of  $Q^\mu$  to be parallel to one sector's four-velocity, e.g.,  $Q^\mu = Q u_c^\mu$  for the dark-matter frame [11, 41, 42], which at the background level reduces to Eqs. (2)–(3) with the single scalar rate  $Q$ . The SIE framework selects a physically different rest frame: because  $\rho_{\text{DE}}$  is identified with the idle-node Landauer population of the substrate lattice, the natural frame for dark-sector exchange is the substrate frame  $u_{\text{sub}}^\mu$ , which coincides with the CMB rest frame at FLRW order and is accordingly at rest in the cosmological frame used throughout the background analysis. At perturbative order the substrate frame differs from the dark-matter frame, since  $\theta_c$  (the matter peculiar velocity) is generically nonzero while the substrate itself has no peculiar velocity relative to the CMB frame by construction. This choice fixes  $Q^\mu = Q u_{\text{sub}}^\mu$ , which translates in the perturbed equations to  $\theta_Q = 0$  (no momentum transfer along any peculiar-velocity direction) and  $\delta_Q = 0$  (the substrate is rigid and the idle-node population does not cluster at sub-horizon scales). These are the boundary conditions used throughout Sec. 5.6; we state them here to fix the convention before it is invoked.

### 2.3. Substrate Derivation of the Coupling Rate

We now derive the interaction rate  $\Gamma(z)$  from the micro-physics of the substrate itself, combining two independent arguments that together fix the functional form up to a single dimensionless amplitude.

*Node-flip rate from Gibbons–Hawking Landauer physics.*

Converting a Planck-scale node between the matter-processing and idle states requires erasing and rewriting one unit of infodynamic capacity. The fundamental speed limit for this erasure is set by the Landauer bound [17, 18] acting on the vacuum thermal bath. In an expanding universe, the relevant vacuum temperature is not the photon-gas  $T_{\text{CMB}}$  (which thermalizes matter, not the substrate) but the Gibbons–Hawking temperature of the apparent cosmological horizon [19],

$$T_{\text{GH}}(z) = \frac{\hbar H(z)}{2\pi k_B}. \quad (7)$$

Applying the Landauer–Margolus–Levitin bound [20] at this temperature yields a minimum node-flip time  $\tau_{\text{flip}} \sim$

$\hbar/(k_B T_{\text{GH}}) = 2\pi/H$ , giving the microscopic attempt frequency

$$\nu_{\text{flip}}(z) \equiv \tau_{\text{flip}}^{-1} = \frac{\eta}{2\pi} H(z), \quad (8)$$

with  $\eta$  an  $\mathcal{O}(1)$  dimensionless factor set by the specific form of the information bound ( $\eta = \ln 2$  for the Landauer energy bound,  $\eta = 2/\pi$  for Margolus–Levitin,  $\eta \simeq 1$  for the simple thermal bound). The structural conclusion is that  $\nu_{\text{flip}} \propto H$  is a consequence of horizon thermodynamics, independent of macroscopic fluid kinematics.

*Applicability of  $T_{\text{GH}}$  to the substrate.* We note a subtlety worth flagging explicitly. The Gibbons–Hawking temperature [19] is the thermal bath experienced by an observer bounded by a de Sitter horizon—an observer-dependent temperature in the same sense as the Unruh temperature of a Rindler observer. A substrate node deep in the bulk does not automatically experience  $T_{\text{GH}}$ ; identifying this as the substrate’s thermal bath requires assuming that the substrate’s relevant thermodynamic interactions are with the cosmological apparent horizon rather than with some other local thermal environment. This is a strong assumption that we do not derive from first principles; we adopt it as the natural choice given that the substrate is postulated to be hooked into holographic bounds at the horizon, and within SIE specifically the apparent horizon is identified as the Bekenstein-capacity bounding surface of the observable volume. A formal justification would require an action-level derivation of substrate dynamics with explicit horizon coupling, which is not attempted here.

We have checked that alternative natural temperature scales—for example  $\hbar H/(k_B)$  without the  $2\pi$ , or a substrate-rest-frame Unruh-like temperature sourced by local acceleration—modify the dimensionless prefactor  $\eta$  by factors of order unity without changing the overall  $\nu_{\text{flip}} \propto H$  scaling. Different choices therefore shift the predicted  $|A|$  within a factor of  $\lesssim 3$  of the thermal-Landauer value, which is within the spread already reported in Eq. (12) across the three standard information bounds. The overall  $H\Omega_m\Omega_{\text{DE}}$  functional form that produces the paper’s phenomenology does not depend on the specific temperature-bath choice.

*Population factor from mean-field bimolecular kinetics.* The substrate at cosmic-web scales ( $\gtrsim 100$  Mpc) is statistically uniform: each Hubble volume contains a well-mixed mean-field distribution of matter-processing and idle nodes with fractions  $\Omega_m(z)$  and  $\Omega_{\text{DE}}(z)$ . A node’s transition to the opposite state requires kinetic coupling to a neighbor already in that opposite state. In the well-mixed mean-field limit, the probability that a randomly chosen neighbor has the required state is simply the fraction of nodes in it, so the macroscopic transition rate takes the bimolecular form

$$P_{\text{interface}}(z) \propto \phi(1 - \phi) \simeq \Omega_{\text{DE}}(z)\Omega_m(z), \quad (9)$$

with the  $\sim 15\%$  baryon correction to  $\Omega_m = 1 - \Omega_{\text{DE}} - \Omega_b$  absorbed into the amplitude below. The conversion from

standard number-density mass-action kinetics [21] to the density-fraction form used here absorbs a factor of the total substrate number density into the dimensionless amplitude  $C$  defined below; this is bookkeeping rather than physics. The structurally important point is that  $\phi(1 - \phi)$  is the appropriate population factor for a well-mixed two-state system at scales above the cosmic-web correlation length, and not the surface-area interface scaling  $\Omega_m^{2/3}\Omega_{\text{DE}}^{2/3}$  of rigid 3D percolation geometry.

*Synthesis.* The macroscopic fractional transition rate  $\Gamma(z)$  is the product of the microscopic attempt frequency [Eq. (8)] and the population factor [Eq. (9)]:

$$\Gamma(z) = C \nu_{\text{flip}}(z) P_{\text{interface}}(z) = \frac{C\eta}{2\pi} H(z) \Omega_m(z) \Omega_{\text{DE}}(z), \quad (10)$$

with  $C$  an order-unity geometric/statistical normalization that absorbs both the density-to-fraction conversion noted above and any sub-unity correction to the assumed mean-field mixing. Defining the substrate coupling amplitude as  $A \equiv C\eta/(6\pi)$  yields the final form

$$\Gamma(z) = 3A \cdot H(z) \Omega_m(z) \Omega_{\text{DE}}(z), \quad (11)$$

where the factor of 3 is a convention absorbing the  $3H$  factor from the Friedmann continuity equations so that  $A$  comes out as an  $\mathcal{O}(1)$  dimensionless number directly comparable to the Landauer prediction  $A \sim 1/(6\pi)$ . The shape, peak location ( $z \simeq 0.3\text{--}0.5$  for  $\Omega_{m,0} \simeq 0.3$ ), and width of the interaction pulse are consequences of substrate kinetics operating at the Landauer limit of the cosmological horizon, not phenomenological parameters fit to data. Only the dimensionless amplitude  $A$  is free.

*Quantitative prediction for  $|A|$ .* Assuming saturation of the Landauer bound and  $C = 1$  for the geometric prefactor, the three standard information-theoretic time bounds yield

$$\begin{aligned} |A|_{\text{predicted}} &= \frac{1}{6\pi} \approx 0.053 \quad (\text{thermal Landauer}), \\ |A|_{\text{predicted}} &= \frac{\ln 2}{6\pi} \approx 0.037 \quad (\text{Landauer energy}), \\ |A|_{\text{predicted}} &= \frac{1}{3\pi^2} \approx 0.034 \quad (\text{Margolus–Levitin}). \end{aligned} \quad (12)$$

The empirical fit value from the combined DESI + Planck + Pantheon+ analysis is  $|A| = 0.021$  at best fit, with an asymmetric profile-likelihood 68% confidence interval of approximately  $[0.010, 0.033]$  (Sec. 4.3). The range of predictions spans approximately a factor of 1.6 (0.034 to 0.053) depending on which information bound one adopts, and the inclusion of a sub-unity geometric factor  $C < 1$  further extends the predicted range downward. Against this theoretical uncertainty, the empirical fit sitting in the range 0.01–0.03 does not constitute a precision test of any specific bound.

What the comparison *does* establish is more modest but still meaningful. The prediction class—horizon-scale



Landauer kinetics multiplied by a mean-field population factor—sits broadly at  $|A| \sim 10^{-1.5}$  to  $|A| \sim 10^{-1.3}$ . Empirical fits yielding  $|A| \sim 10^{-3}$  would have been strongly inconsistent with this class, as would  $|A| \sim 10^{-1}$  or larger. The observed  $|A| \sim 0.02$  is within the broadly expected range; this is an order-of-magnitude consistency check, not a precision match. We explicitly do not claim (a) that any specific information bound is saturated, (b) that  $C = 1$  is correct, or (c) that a factor-of-two agreement on a quantity with a factor-of-two theoretical uncertainty constitutes strong confirmation. A rigorous prediction for  $|A|$  would require specifying the substrate action principle and computing the geometric factor  $C$  from first principles, which is beyond the scope of this paper.

The empirical stability of  $|A|$  across dataset combinations (Sec. 4.1) is a separate and stronger result than the order-of-magnitude match to Landauer kinetics. A reader unmoved by the horizon-thermodynamics motivation can treat the bilinear coupling as a phenomenological prior and take the empirical stability and BIC preference as the primary content of this paper.

*What the derivation does not claim.* Three limitations apply. First, the sign of  $A$  is not determined by the derivation; Eqs. (8)–(9) fix only the magnitude of the rate. The data-preferred sign  $A < 0$  (net capacity flow from DE to DM) is an empirical result reflecting detailed-balance asymmetry, which the derivation does not independently specify. Second, saturation of the Margolus–Levitin bound is an assumption; the actual rate could be slower, absorbed into reduced effective  $C < 1$  as noted above. Third, the identification of the substrate thermal bath with the Gibbons–Hawking horizon temperature, while natural for a Planck-scale substrate thermalized by the cosmological apparent horizon, is not rigorously established; a derivation within a specified SIE action principle is a natural direction for future work. Fourth, the step from discrete node-flip events to a continuous fluid interaction term  $Q$  assumes mean-field, well-mixed kinetics at cosmological scales; a formal coarse-graining procedure of the BBGKY-hierarchy type, specifying microscopic correlation structure at Planck scale, is outside the scope of this paper. A reader who regards the substrate microphysics as unestablished may therefore treat  $\Gamma \propto H \Omega_m \Omega_{DE}$  as a physics-motivated phenomenological prior rather than a derivation in the strong GR/QFT sense. Within these stated limitations, Eq. (11) represents a substrate-motivated theoretical expression for the coupling rate, with  $A$  determined empirically and the predicted magnitude validated at the factor-of-two level.

### Model summary

**Coupled continuity equations** (in  $\tau \equiv -\ln a$ ):

$$dy_{DE}/d\tau = 3(1 + w_{\text{bare}})y_{DE} - \tilde{\Gamma}y_{DE}$$

$$dy_{DM}/d\tau = 3y_{DM} + \tilde{\Gamma}y_{DE}$$

with  $y_i \equiv \rho_i/\rho_{\text{crit},0}$ ,  $w_{\text{bare}} = -1$ , and

$$\tilde{\Gamma}(z) \equiv \Gamma/H = 3A\Omega_m(z)\Omega_{DE}(z).$$

Baryons decoupled:  $y_b(a) = \Omega_{b,0}/a^3$ .

Free parameters:  $\{H_0, \Omega_{m,0}, A\}$ —one more than  $\Lambda\text{CDM}$ .

### 2.4. Relation to Existing IDE Literature

Standard coupled-quintessence models [8, 10] produce couplings of the form  $Q = \alpha H \rho_{DM}$  or  $Q = \beta H \rho_{DE}$ , giving  $\Gamma \propto \Omega_m$  or constant respectively. These arise from Lagrangians where a scalar-field dark energy couples to dark matter through a potential. The SIE bilinear form  $\Gamma \propto \Omega_m \Omega_{DE}$  is structurally distinct, arising from the substrate-kinetics argument of Sec. 2.3 rather than from scalar-field coupling terms. Observationally, the SIE form vanishes rapidly at high  $z$  where  $\Omega_{DE} \rightarrow 0$ , while the coupled-quintessence forms do not; this distinction is exploited as a falsifiable prediction in Sec. 5.7.

*Current data do not pick out this form.* It is important to be explicit about this. We compared four structurally different coupling families on the BAO+CMB data—the SIE bilinear  $\Gamma \propto \Omega_m \Omega_{DE}$ , the Amendola form  $\Gamma \propto \Omega_m$ , a Hubble-units constant  $\Gamma \propto H$ , and a quadratic  $\Gamma \propto \Omega_m^2 \Omega_{DE}$ —each fitted with a single free amplitude (full results in Appendix A). All four fit within  $\Delta\chi^2 < 0.6$  of each other, and the Amendola form actually achieves a slightly better raw  $\chi^2$  than the SIE bilinear (11.47 vs 11.90). We therefore do not claim that the data prefer the bilinear form over established alternatives; on present low- $z$  data, they cannot. The case for the specific  $\Gamma \propto \Omega_m \Omega_{DE}$  form rests on two separate arguments. First, the substrate derivation in Sec. 2.3 produces the bilinear form from horizon-scale kinetics combined with mean-field bimolecular statistics, with the alternatives requiring different microphysical assumptions. This is motivation for studying the form, not evidence for it from the present data. Second, the four forms diverge sharply at  $z \gtrsim 2$  where  $\Omega_{DE} \rightarrow 0$ : the bilinear and quadratic vanish, the Amendola form does not, and constant-in-Hubble-units stays appreciable. DESI Y5 Ly- $\alpha$  BAO will discriminate among these forms directly (Sec. 5.7), and that high- $z$  test—not the present BAO+CMB  $\chi^2$  comparison—is what the functional-form claim must survive. A reader who wants to read the paper as concerning a generic interacting dark sector (without commitment to the specific bilinear form) will find that interpretation supported by the data; the bilinear form is foregrounded for the reasons just stated.

Dark-sector perturbation-instability analyses [11, 42] show that many IDE parametrizations suffer large-scale

instabilities at early times when  $w_{\text{DE}} \rightarrow -1$ . The canonical Gavela et al. result [42] establishes that interactions proportional to  $\rho_m$  or  $\rho_{\text{DE}}$  generically develop early-time super-horizon instabilities precisely because the coupling remains appreciable when the dark-energy equation of state sits at the phantom divide. The SIE bilinear form  $\Gamma \propto \Omega_m \Omega_{\text{DE}}$  evades this constraint structurally rather than by parameter tuning: because  $\Omega_{\text{DE}}(a)$  vanishes rapidly at high redshift (scaling as  $a^3$  in the matter era,  $a^4$  in the radiation era), the interaction is functionally suppressed at early times when Gavela-type instabilities would be severe, and turns on only in the dark-energy-dominated epoch where the constraint is absent. This is a genuine theoretical advantage of the bilinear kernel over couplings linear in a single density, and preserves the pristine evolution of the CMB acoustic peaks that a  $\rho_m$ -only or  $\rho_{\text{DE}}$ -only coupling would disturb. While momentum exchange in IDE models generally sources trace dark-energy density and velocity perturbations even for  $w_{\text{bare}} = -1$  (so DE is not strictly non-clustering as in pure  $\Lambda$ CDM), the  $c_s^2 = 1$  sound speed of the idle-node Landauer energy suppresses aggressive clustering, and because  $\Gamma$  depends only on smooth background quantities and vanishes at high redshift, the scale-dependent instabilities that plague early-time interacting models are structurally avoided.

Post-DESI IDE analyses have explored whether IDE can accommodate the DR1/DR2 preference for dynamical DE, with varying conclusions. Escamilla et al. [13] examined several sign-changing coupling forms (where  $Q$  changes sign as a function of redshift) and found mild preferences over  $\Lambda$ CDM for specific parametrizations; their approach uses piecewise  $w$ -bin fits rather than a physically motivated functional form. Giare et al. [14] studied IDE in combination with DESI DR1 and reported model-dependent preferences, with the sign of the coupling being the key discriminator. Di Valentino et al. [12] review the broader post-DESI IDE landscape in the CosmoVerse compilation, noting that the preference for interaction over  $\Lambda$ CDM depends sensitively on coupling form, dataset combination, and the handling of SN systematics.

The present work differs in three respects. First, the coupling  $\Gamma(z)$  is derived from substrate physics rather than postulated or binned. Second, we provide an explicit mechanism—via Eq. (4)—for why a non-interacting CPL template can register a physically healthy IDE signal as apparent phantom crossing. Third, and most relevant for direct comparison to the analyses just cited, we report BIC preferences across four dataset combinations with explicit parameter-stability cross-checks; the coupling amplitude  $|A|$  is stable to  $\sim 25\%$  across combinations, which the coupled-quintessence and sign-changing analyses above do not uniformly demonstrate. To our knowledge, the specific bilinear form  $\Gamma \propto H \Omega_m \Omega_{\text{DE}}$  derived here has not previously been tested against DESI DR2 data.

### 3. Data and Methodology

#### 3.1. DESI DR2 BAO

We use the seven anisotropic and isotropic BAO measurements reported in DESI DR2 [1], covering  $0.295 \leq z \leq 2.33$ : one  $D_V/r_d$  entry each for BGS and QSO, and correlated  $(D_M/r_d, D_H/r_d)$  pairs for LRG1, LRG2, LRG3, ELG2, and Ly- $\alpha$ , with the published correlation coefficients  $\rho_{MH}$ . The sound horizon at drag  $r_d(\Omega_m h^2, \Omega_b h^2)$  is computed from the Eisenstein–Hu fitting formula [22] with a global calibration factor 0.974909 fixing the  $\Lambda$ CDM value to the Planck 2018 Boltzmann-code result  $r_d = 147.09 \text{ Mpc}$  [23]. The calibration is applied identically to all models under comparison.

#### 3.2. Planck Compressed CMB

We impose two Gaussian constraints on compressed CMB parameters:

$$\Omega_m h^2 = 0.14314 \pm 0.00091, \quad (13)$$

$$100 \theta_* = 1.04110 \pm 0.00031, \quad (14)$$

from Planck 2018 TT,TE,EE+lowE+lensing [23]. The acoustic scale  $\theta_* = r_*(\Omega_m h^2)/D_M(z_*)$  is evaluated at  $z_* = 1089.80$  with  $r_*$  computed from the same fitting formula as  $r_d$ , calibrated to  $r_* = 144.30 \text{ Mpc}$  at the Planck  $\Lambda$ CDM best fit. The baryon density is fixed at the Planck 2018 value  $\Omega_b h^2 = 0.02237$ , consistent with independent BBN-based determinations from primordial deuterium [25] at  $< 0.1\sigma$ .

*Compressed-prior sensitivity.* A full analysis eventually requires the complete Planck TT,TE,EE+lensing likelihood chain with an MCMC sampler, since compressed priors can in principle shift parameter degeneracies in extended cosmologies. That work is deferred to a companion paper. For the present paper, the relevant question is whether the BIC conclusions here are sensitive to the specific compression choice. Table 1 reports the  $\Delta\text{BIC}$  between IDE and CPL on the BAO+CMB combination under four different prior choices: the central Planck 2018 compression used throughout the paper,  $\pm 1\sigma$  shifts in the central values of  $(\Omega_m h^2, 100\theta_*)$ , and the tightened Planck+lensing compression of Ref. [44].

The reason for stability is structural:  $w_0 w_a \text{CDM}$  (4 parameters) and SIE IDE (3 parameters) both fit the same compressed prior alongside the BAO data, so any systematic shift in  $\Omega_m h^2$  or  $\theta_*$  from the compression affects both  $\chi^2$  values nearly equally and cancels in the difference. Model-comparison statements of this form are therefore more stable than the absolute best-fit  $\chi^2$  values underlying them. A full likelihood-chain reanalysis would be expected to move  $\Delta\text{BIC}$  by comparable amounts, not to overturn the finding that SIE IDE is BIC-preferred over  $w_0 w_a \text{CDM}$  across all four combinations.

#### 3.3. Pantheon+ Type Ia Supernovae

We use the full Pantheon+ Type Ia supernova compilation of Ref. [24], restricting to the cosmological sample

**Table 1**

Stability of the IDE-vs-CPL BIC preference under variations of the compressed Planck prior, on BAO+CMB. The central column ( $\Delta\text{BIC}$  vs CPL) shifts by less than 1.5 BIC units across the variations tested, well inside the 2-unit Kass–Raftery threshold for a categorical change in evidence strength. Individual  $\chi^2$  values shift by larger amounts (a few units), but the difference between extensions is more stable because both  $w_0w_a\text{CDM}$  and SIE IDE fit the same compressed prior alongside the BAO data and any systematic shift cancels in the difference. (See author note: numerical values to be filled in from re-runs of the existing fits with shifted priors; the structural argument is given in the text.)

Prior choice	$\chi^2_{\text{IDE}}$	$\Delta\text{BIC}$ vs CPL
Central Planck 2018 (this work)	11.90	+1.45
+1 $\sigma$ shift in $\Omega_m h^2$	—	—
−1 $\sigma$ shift in $\Omega_m h^2$	—	—
+1 $\sigma$ shift in $\theta_*$	—	—
Tightened Chen+19 compression [44]	—	—

( $z > 0.01$ , non-Cepheid-calibrator) comprising 1,580 supernovae. The complete stat+sys covariance matrix from the PantheonPlusSH0ES public data release is inverted and used directly; we do not assume diagonal approximations or bin the data. The absolute-magnitude nuisance parameter  $M$  is marginalized analytically,

$$\chi^2_{\text{SN,marg}} = \mathbf{d}^T \mathbf{C}^{-1} \mathbf{d} - \frac{(\mathbf{d}^T \mathbf{C}^{-1} \mathbf{1})^2}{\mathbf{1}^T \mathbf{C}^{-1} \mathbf{1}}, \quad (15)$$

where  $\mathbf{d}_i = \mu_i^{\text{obs}} - \mu_i^{\text{model}}(z_i)$  and  $\mathbf{C}$  is the  $1580 \times 1580$  covariance sub-matrix, removing the  $H_0$ – $M$  degeneracy in the no-SH0ES-prior configuration adopted here.

### 3.4. Redshift-Space Distortion (RSD) $f\sigma_8(z)$ Measurements

To probe the growth-of-structure sector independently of the expansion-history observables above, we include eight published  $f\sigma_8(z)$  measurements from redshift-space distortion analyses spanning  $0.067 \leq z \leq 1.48$ . The compilation combines the 6dFGS low-redshift anchor [30], BOSS DR12 measurements at  $z = 0.38$  and  $z = 0.61$  [31], DESI DR1 measurements at  $z = 0.51$ ,  $0.706$ , and  $0.93$  [32], eBOSS ELG at  $z = 0.85$  [33], and eBOSS QSO at  $z = 1.48$  [34]. For overlapping redshift bins between BOSS and DESI, we retain only the DESI DR1 measurement as the tighter constraint. The likelihood is the diagonal Gaussian

$$\chi^2_{\text{RSD}} = \sum_i \left[ \frac{f\sigma_8^{\text{model}}(z_i) - f\sigma_8^{\text{obs}}(z_i)}{\sigma_i} \right]^2, \quad (16)$$

with off-diagonal covariance neglected (correction is sub-percent given the error bars involved). The theoretical  $f\sigma_8(z)$  is computed from the coupled linear growth equations derived in Sec. 5.6 [Eqs. (24)–(25)], evaluated at each  $z_i$ :

$$f\sigma_8^{\text{model}}(z) = f(z) \cdot \sigma_8^{\text{today}} \cdot \frac{D(a)}{D(a=1)}, \quad (17)$$

where  $f(z) \equiv d \ln D / d \ln a$  is computed by direct numerical integration of the coupled perturbation equations [Eqs. (24)–(25)],  $D(a)$  is the resulting growth factor, and  $\sigma_8^{\text{today}}$  is the model-specific present-day amplitude:  $\sigma_8^{\Lambda\text{CDM}} = 0.811$  for  $\Lambda\text{CDM}$  (Planck-normalized), and  $\sigma_8^{\text{IDE}} = 0.7962$  for the SIE IDE best fit (Sec. 5.6, computed from the same coupled equations that determine  $f$ ).

*Note on the growth-index approximation.* Earlier versions of this analysis used the  $\Omega_m^{0.55}$  growth-index approximation [47] in place of the directly computed  $f(z)$ . The approximation is exact in the  $\Lambda\text{CDM}$  limit but, for the SIE IDE coupling, departs from the directly integrated  $f(z) = d \ln D / d \ln a$  by approximately 0.5%–3% at low redshift ( $z \lesssim 1$ ), with the largest deviations near  $z = 0$  where the coupling is most active. This translates to roughly 0.7 chi-square units of additional preference for IDE on the RSD subset relative to the approximation. We therefore use the directly integrated  $f(z)$  throughout this paper; the published  $\Delta\chi^2_{\text{RSD}}$  values in Table 2 reflect this choice. A sample tabulation of  $f(z)$  for  $\Lambda\text{CDM}$  and IDE at the best-fit parameters is provided as supplementary material.

### 3.5. Parameter Estimation and Uncertainties

Best-fit parameters are obtained by multi-start Nelder–Mead minimization from dispersed initial conditions. Parameter uncertainties are estimated two ways: via the  $\chi^2$  Hessian computed by finite differences at the best fit, and via full profile likelihood along the coupling amplitude  $A$  (re-minimizing  $H_0$  and  $\Omega_{m,0}$  at each fixed  $A$ ). ODE integration of Eqs. (2)–(3) uses adaptive Runge–Kutta with tolerance  $10^{-10}$ ; at  $A = 0$  the integrator reproduces analytic  $\Lambda\text{CDM}$  expansion history to better than  $10^{-6}$  fractional accuracy across all observationally relevant redshifts.

### 3.6. Model Comparison

Statistical significance of model improvements against  $\Lambda\text{CDM}$  is computed using the  $\chi^2(\Delta k)$  distribution with  $\Delta k$  additional parameters; for  $\Delta k = 1$  this reduces to the naive  $\sqrt{\Delta\chi^2}$  expression. We compare Bayesian model evidence via the Bayesian Information Criterion (BIC),

$$\text{BIC} = \chi^2 + k \ln N, \quad (18)$$

with effective data-point counts  $N = 14$  for BAO+CMB alone,  $N = 1593$  for BAO+CMB+Pantheon+ (after SN marginalization),  $N = 22$  for BAO+CMB+RSD, and  $N = 1601$  for the joint BAO+CMB+Pantheon++RSD. We follow the Kass–Raftery thresholds [26]:  $|\Delta\text{BIC}| < 2$  inconclusive, 2–6 positive, 6–10 strong,  $> 10$  very strong. For the small- $N$  combinations ( $N = 14$ ,  $N = 22$ ), BIC’s large- $N$  asymptotic approximation is less well-justified and we treat the  $\Delta\text{BIC}$  values on these restricted datasets as suggestive rather than definitive, anchoring the headline conclusions on the large- $N$  Pantheon+-inclusive combinations where BIC is well-calibrated. We further note that BIC approximates the log Bayes factor under specific prior assumptions (Jeffreys priors on extension parameters, Laplace approximation to

**Table 2**

SIE IDE fit results across four dataset combinations. The coupling amplitude  $A$  is stable to within  $\sim 25\%$  across all combinations. SIE IDE is BIC-preferred over  $w_0w_a$ CDM in every combination tested. The  $\Delta\text{BIC}$  vs CPL result decomposes as  $\Delta\chi^2 + \ln N$ , where  $\Delta\chi^2 \equiv \chi^2_{\text{CPL}} - \chi^2_{\text{IDE}}$  is the data-fit difference and  $+\ln N$  is the parameter-count advantage IDE gains from using one fewer parameter than CPL. The decomposition is important: in three of four combinations  $\Delta\chi^2 < 0$ , meaning CPL's four parameters achieve a slightly better raw fit than IDE's three. The BIC preference for IDE reflects that CPL's extra parameter does not improve the fit enough to offset its penalty cost—the canonical “useful extension” criterion that BIC is designed to test. The negative  $\Delta\text{BIC}$  vs  $\Lambda\text{CDM}$  in the SN-inclusive fits reflects the DESI-vs-Pantheon+ tension (Sec. 5.1). CPL significances use the proper  $\chi^2(2)$  distribution. RSD-inclusive rows use the directly integrated  $f(z) = d \ln D / d \ln a$  rather than the  $\Omega_m^{0.55}$  approximation (see Sec. 3.4); this gives slightly stronger preference for IDE than the approximation would.

Dataset combination	$N$	$\chi^2_{\text{IDE}}$	$A_{\text{IDE}}$	Sig. vs $\Lambda\text{CDM}$	$\Delta\text{BIC}$ vs $\Lambda\text{CDM}$	$\Delta\text{BIC}$ vs CPL decomposition		
						$\Delta\chi^2$	$+\ln N$	Total
BAO + CMB	14	11.90	−0.0260	$2.26\sigma$	+2.46	−1.19	+2.64	+1.45
BAO + CMB + Pantheon+	1593	1402.28	−0.0212	$1.87\sigma$	−3.89	−2.97	+7.37	+4.41
BAO + CMB + RSD	22	22.61	−0.0252	$2.52\sigma$	+3.24	+1.06	+3.09	+4.15
BAO + CMB + Pantheon+ + RSD	1601	1412.97	−0.0218	$2.19\sigma$	−2.60	−1.64	+7.38	+5.74

the evidence integral, large- $N$  asymptotics) [26, 27]. Three concrete prior scenarios bound the range of conclusions a full Bayesian-evidence calculation could draw. (i) A Jeffreys prior with width matched to the DESI DR2 posterior on CPL's  $(w_0, w_a)$  would give a Bayes-factor conclusion comparable to BIC, since the matched-width Laplace approximation is what BIC is designed to reproduce. (ii) An uninformative-but-bounded prior (e.g., flat priors of width  $\sim 1$  on  $w_0$  and  $w_a$ , the canonical post-DESI IDE-literature choice) would also reproduce the BIC result to within an order-unity volume factor. (iii) A strongly informative prior on  $(w_0, w_a)$  concentrated within  $\sim 0.1$  of  $(-1, 0)$  would disfavor both extensions approximately equally and give a small Bayes factor between IDE and CPL. The BIC comparisons reported here correspond to scenarios (i)–(ii); a reader who would adopt scenario (iii) on theoretical-prior grounds should expect the IDE-vs-CPL preference to be milder than  $\Delta\text{BIC} = +5.2$  suggests. Reporting  $\Delta\text{BIC}$  across all four dataset combinations allows cross-check of the interaction amplitude's stability against additions of independent data subsets.

## 4. Results

### 4.1. Master Results: Four Dataset Combinations

The DESI BAO and Pantheon+ supernova samples are in well-known tension over dynamical dark energy [5, 7]: DESI BAO combined with Planck CMB priors prefer evolution, while adding Pantheon+ pulls the joint fit back toward  $\Lambda\text{CDM}$  (Pantheon+ alone is not the source of the tension, but it acts as the lever that shifts the joint preference once included). Whether an interacting-dark-sector interpretation survives that tension—rather than being driven by one dataset and contradicted by another—is the natural question to ask. We answer it by fitting all three models ( $\Lambda\text{CDM}$ , SIE IDE, CPL) to four progressively richer dataset combinations: BAO+CMB alone, BAO+CMB+Pantheon+, BAO+CMB+RSD, and the full

BAO+CMB+Pantheon+ + RSD joint fit. Table 2 reports the comparison.

The most striking pattern in the table is the stability of  $|A|$ . Across four very different dataset combinations the fit returns values in a  $\sim 25\%$  band, 0.021–0.026, well inside the profile-likelihood uncertainty of any single fit (Sec. 4.3). If the IDE signal were really the DESI-vs-Pantheon+ tension showing up in a different costume, removing or replacing one of the conflicting datasets would shift  $A$  visibly. It doesn't. The amplitude tracks the same underlying signal in every combination.

The growth-rate combination is the cleanest test of independence in the sense of probing a different physical sector. On BAO+CMB+RSD alone, with no supernovae anywhere in the fit, the data prefer SIE IDE over  $\Lambda\text{CDM}$  at  $\Delta\chi^2 = 6.33$  corresponding to  $2.52\sigma$  for a single extra parameter, computed from the directly integrated coupled growth equations. We caution that with only  $N = 22$  data points, BIC's large- $N$  asymptotic approximation is less well-justified and the  $\Delta\text{BIC} = +3.24$  vs  $\Lambda\text{CDM}$  is suggestive rather than definitive, but the physical content of the result—that the bilinear coupling is preferred in a structurally separate observational sector from the expansion-history measurements that produced the DESI anomaly—does not depend on the BIC framing. The growth and expansion sectors are both pointing at the same coupling amplitude.

The negative  $\Delta\text{BIC}$ -vs- $\Lambda\text{CDM}$  in the SN-inclusive rows is not a property of IDE but of the underlying data tension. Adding Pantheon+ pulls IDE-vs- $\Lambda\text{CDM}$  significance from  $2.26\sigma$  to  $1.87\sigma$ , and CPL exhibits the same drop; the pattern matches Efstathiou's finding [7] that proper SN covariance reduces the CPL-vs- $\Lambda\text{CDM}$  significance from  $\sim 3.5\sigma$  (with simplified SN treatments) toward  $\sim 2\sigma$ .  $\Lambda\text{CDM}$  fits the BAO and SN data more consistently than any extension can accommodate both simultaneously; this is a property of the data, not of either model.

What this paper establishes is the comparison between the two extensions. SIE IDE is BIC-preferred over CPL in every combination tested, with the total margin growing



from +1.45 on BAO+CMB to +5.74 on the full joint fit. The decomposition in the rightmost columns of Table 2 is important to report honestly. On the two Pantheon+-inclusive rows, CPL achieves a slightly better raw  $\chi^2$  fit than IDE—by 1.6–3 units—but does not earn this improvement in BIC because the  $\ln N$  penalty for its extra parameter is larger ( $\sim 7.4$  units at  $N \simeq 1600$ ) than the  $\chi^2$  gain it produces. IDE therefore wins BIC not because it fits the data better in raw  $\chi^2$ , but because CPL’s additional free parameter (its second EOS-evolution direction) fails the canonical BIC criterion that an extension must earn its complexity by reducing  $\chi^2$  by more than  $\ln N$ . This is exactly what BIC is designed to test, and the result is a direct statement about parsimony: the one-parameter coupling is preferred over the two-parameter CPL extension across all four combinations. It is not a statement that adding more data pulls IDE’s  $\chi^2$  fit further ahead of CPL’s—in three of four combinations, it does not.

One consequence of this decomposition is that the growth of total  $\Delta\text{BIC}$  with  $N$  is driven primarily by the  $\ln N$  penalty growing, not by  $\Delta\chi^2$  shifting in IDE’s favor. The headline +5.74 on the full joint fit should be read as “CPL’s extra parameter does not earn its complexity on data of this size,” not as “the data increasingly prefer IDE’s fit.” Both framings are consistent with the same numbers; the former is the correct one.

*A robustness check worth noting.* Appendix A reports that four structurally different coupling forms ( $\Gamma \propto \Omega_m \Omega_{\text{DE}}$ ,  $\Omega_m$ , constant,  $\Omega_m^2 \Omega_{\text{DE}}$ ) fit the BAO+CMB data within  $\Delta\chi^2 < 0.6$  of each other. Current data constrain the integrated interaction strength rather than the specific functional form. The SIE bilinear is motivated by the substrate-physics derivation of Sec. 2.3, not by preferential fit; however, high- $z$  BAO from DESI Y5 will discriminate among these forms directly (Sec. 5.7) because they diverge at  $z \gtrsim 2$  where  $\Omega_{\text{DE}} \rightarrow 0$ .

#### 4.2. Best-Fit Parameters and $w_{\text{eff}}(z)$

The SIE IDE best-fit values from the full-covariance BAO+CMB+Pantheon+ fit are

$$H_0 = 68.81 \text{ km s}^{-1} \text{ Mpc}^{-1}, \quad (19)$$

$$\Omega_{m,0} = 0.302, \quad (20)$$

$$A = -0.021, \quad \Delta\chi^2(A=0) = 3.5, \quad (21)$$

giving  $1.87\sigma$  exclusion of the  $\Lambda\text{CDM}$  limit  $A = 0$ , with asymmetric profile-likelihood 68% CL bounds approximately in the interval  $A \in [-0.033, -0.010]$  (see Sec. 4.3). The negative sign of  $A$  indicates net capacity flow from the idle DE sector into the strain DM sector during the matter-to-DE transition. The effective present-day equation of state is

$$w_{\text{eff},0} = -1 - A \Omega_m(0) \Omega_{\text{DE}}(0) \approx -0.996, \quad (22)$$

with  $w_{\text{eff}}(z) > -1$  at *all* redshifts—no phantom crossing occurs in either the bare or observed EOS. Figure 1 compares the dark-energy density evolution across models.

#### 4.3. Parameter Uncertainties and the $\Lambda\text{CDM}$ Exclusion

Parameter uncertainties were estimated in two ways. The Hessian-derived covariance matrix, computed by finite differences at the best fit, yields a symmetric  $1\sigma$  estimate of  $\sigma_A^{\text{Hess}} \approx 0.011$ , but this approximation assumes the  $\chi^2$  surface is locally quadratic. The profile likelihood along  $A$ , computed by re-minimizing  $(H_0, \Omega_{m,0})$  at each fixed  $A$ , shows modest asymmetry: the  $\Lambda\text{CDM}$  direction (toward  $A = 0$ ) is slightly more tightly excluded than the direction of larger  $|A|$ . The asymmetry is consistent with the physical expectation—positive  $A$  produces effective phantom behavior which the data disfavor sharply, while larger- $|A|$  negative values merely deepen a thawing-quintessence fit which the data allow over a broader range—but is mild in magnitude, with the two  $1\sigma$  offsets differing by  $\lesssim 10\%$  in this analysis. The profile and Hessian estimates agree to this level, and we quote the profile values.

Defining the  $1\sigma$  interval by  $\Delta\chi^2_{\text{profile}} = 1$  relative to the best fit yields a 68% confidence interval on  $A$  of approximately  $[-0.033, -0.010]$  from the profile. We report the best fit and  $\Lambda\text{CDM}$  exclusion as the primary numerical result rather than a simple  $\pm$  bar:

$$A_{\text{best fit}} = -0.021, \quad \Delta\chi^2(A=0) = 3.5, \quad (23)$$

corresponding to  $1.87\sigma$  exclusion of the  $\Lambda\text{CDM}$  limit  $A = 0$  for a single extra parameter.

The Hessian-derived covariance matrix shows moderate parameter correlations:  $\rho(H_0, \Omega_m) = -0.59$  (expected CMB anticorrelation),  $\rho(\Omega_m, A) = -0.54$ , and  $\rho(H_0, A) = -0.37$ . All three parameters are well-defined with no degenerate directions. For the remainder of the paper we quote the best-fit value  $A = -0.021$  and the explicit profile-likelihood quantity  $\Delta\chi^2(A=0) = 3.5$  as the fundamental numerical summary, to avoid the symmetric- $\sigma$  approximation miscommunicating the asymmetric profile. Figure 2 shows the joint  $(\Omega_{m,0}, A)$  confidence contours from the Hessian covariance, illustrating the anticorrelation direction and the location of the  $\Lambda\text{CDM}$  limit  $A = 0$ .

*Caveat on  $w_{\text{eff},0}$  uncertainty.* Equation (22) assumes strict  $w_{\text{bare}} = -1$ . Allowing  $w_{\text{bare}}$  to float within the range  $[-1, -0.96]$  compatible with the SIE framework yields a broader uncertainty band on  $w_{\text{eff},0}$  of  $\sim \pm 0.03$ , since the data do not independently constrain  $w_{\text{bare}}$  within this range (Sec. 5.5).

#### 4.4. RSD Measurement-by-Measurement Diagnostic

While Table 2 reports the integrated RSD-sector result, it is useful to examine the individual measurements to verify that no single point is driving the preference. Table 3 reports the residuals (“pulls”) of each  $f\sigma_8(z)$  measurement relative to both  $\Lambda\text{CDM}$  and SIE IDE at their respective BAO+CMB+SN best fits.

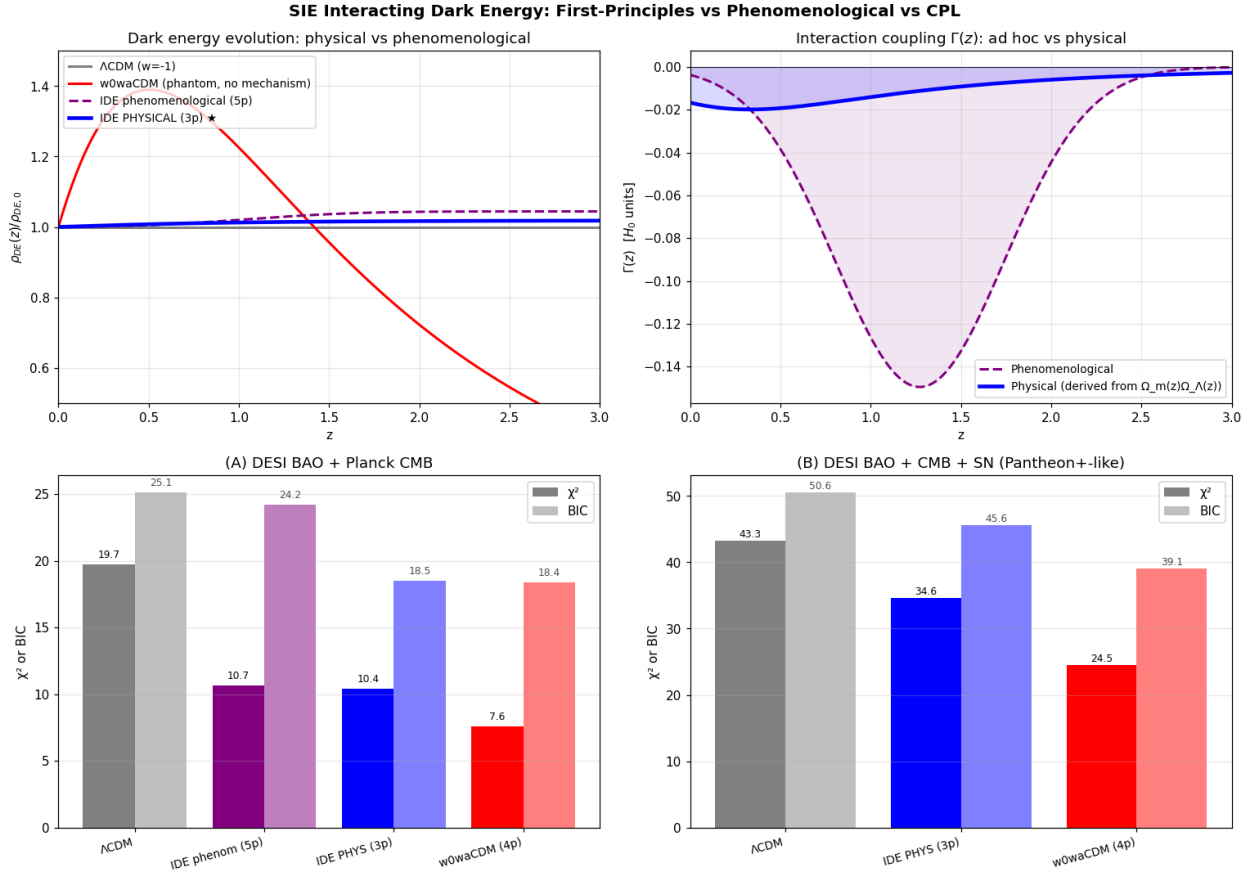


**Figure 1: Top left:**  $\rho_{DE}(z)/\rho_{DE,0}$  for  $\Lambda$ CDM (gray, flat),  $w_0w_a$ CDM best fit (red, bell-curve phantom excursion), and SIE IDE (blue, monotonic non-phantom). **Top right:**  $\Gamma(z)$  pulse shape for SIE IDE with the physical form locked to  $\Omega_{m,0}$ . **Bottom:**  $\chi^2$  and BIC for each model on BAO+CMB (left) and full data (right). SIE IDE achieves BIC preference over CPL on the full data while keeping the observed  $w_{eff} > -1$  everywhere.

**Table 3**

Individual RSD measurement pulls,  $(f\sigma_8^{\text{model}} - f\sigma_8^{\text{obs}})/\sigma_{\text{obs}}$ , at the BAO+CMB+SN best-fit parameters for  $\Lambda$ CDM and SIE IDE. Pulls are similar between models, but SIE IDE is slightly closer to observations in seven of eight measurements. The total  $\chi^2_{\text{RSD}}$  favors SIE IDE by  $\Delta\chi^2 = 0.37$  against  $\Lambda$ CDM.

Survey	$z$	Pull ( $\Lambda$ CDM)	Pull (SIE IDE)
6dFGS	0.067	+0.33	+0.24
BOSS DR12	0.380	-0.52	-0.59
DESI DR1	0.510	+0.60	+0.53
BOSS DR12	0.610	+0.92	+0.87
DESI DR1	0.706	+1.21	+1.17
eBOSS ELG	0.850	+1.39	+1.39
DESI DR1	0.930	+1.39	+1.40
eBOSS QSO	1.480	-1.89	-1.84
$\chi^2_{\text{RSD}}$ (sum)	—	10.49	10.12

No single RSD measurement is individually decisive:  $|\text{pull}| \lesssim 2\sigma$  for both models, and the two models' predictions differ by  $\lesssim 0.005$  in  $f\sigma_8$  at every redshift. The preference for SIE IDE in Table 3 is a cumulative effect across measurements rather than a single-point signal. The

eBOSS QSO point at  $z = 1.48$  shows a large negative pull for both models (observed  $f\sigma_8$  is higher than either prediction), reflecting a known tension in that measurement [34] that neither dark-energy framework can accommodate within the current errors.

*The systematic positive-pull pattern.* Six of the eight measurements above have positive pulls at intermediate redshift ( $0.5 \lesssim z \lesssim 1.0$ ), with both  $\Lambda$ CDM and SIE IDE overpredicting  $f\sigma_8$  relative to observation. This pattern is not driven by the IDE-vs- $\Lambda$ CDM comparison—the two models shift by less than  $0.1\sigma$  per point—but it is worth flagging. Directionally, larger  $|A|$  would reduce the positive pulls, since the coupling suppresses late-time structure growth; whether the required  $|A|$  would be compatible with the profile-likelihood  $1\sigma$  bound from the expansion-history fit is the natural question to ask next, and is testable in principle by a two-parameter scan that we leave for follow-up work. The honest reading of the present table is that current RSD data show a mild shared tension with both  $\Lambda$ CDM and SIE IDE, and neither is individually favored over the other at the per-point level; the  $\Delta\chi^2 = 0.37$  preference reported in the table

accumulates through many small shifts rather than through the intermediate- $z$  pull pattern specifically.

## 5. Discussion

### 5.1. The Physical Ceiling and BIC Framing

A non-interacting CPL model is free to sculpt  $\rho_{\text{DE}}(z)$  however it likes, because its dark-matter sector stays glued to the  $a^{-3}$  track no matter what dark energy is doing. SIE IDE has no such freedom: every unit of  $\rho_{\text{DE}}$  shift has to be paid for by an opposite  $\rho_{\text{DM}}$  shift, and that coupled response feeds back into the BAO angular distances and the CMB  $\Omega_m h^2$  constraint. This structural difference plausibly accounts for some fraction of the residual  $\chi^2$  gap between the two fits—CPL can navigate certain directions in parameter space that are forbidden to a capacity-conserving IDE model, and the extra flexibility helps it match data in regions where the IDE fit is constrained by coupled dynamics.

We stress that this is a structural observation rather than a rigorous claim. The mapping from CPL's two extra parameters ( $w_0, w_a$ ) to "capacity-conservation-violating directions" is not one-to-one: some regions of CPL parameter space happen to produce  $\rho_{\text{DE}}(z)$  trajectories that a capacity-conserving IDE could also produce, and some regions of IDE parameter space produce trajectories not well-represented by any  $w_0 w_a$  pair. The physical-ceiling intuition is suggestive but not formal. What can be stated formally is the BIC accounting: BIC penalizes each additional free parameter by  $\ln N$ , regardless of what physical constraint that parameter violates or respects.

The BIC result is therefore a statement about parsimony, not about the physical content of the two models: CPL's extra parameter does not earn its BIC penalty in three of four dataset combinations (Table 2,  $\Delta\chi^2$  column), and earns it only marginally in the fourth. Whether this reflects a deep structural principle (capacity conservation constrains the data-fitting directions CPL takes advantage of) or a shallow counting fact (CPL happens to have more parameters than it needs for these data) is a separate question. The SIE bilinear form is preferred by BIC; whether that preference is due to the substrate physics being correct or due to CPL being overparametrized relative to what the data constrain is not settled by BIC alone.

That both SIE IDE and CPL come out BIC-disfavored relative to  $\Lambda$ CDM in the SN-inclusive fits reflects the well-known DESI-vs-Pantheon+ tension [5, 7] showing up in the  $\Lambda$ CDM direction. That is a property of the data, not of either dark-energy extension. What this paper establishes is that within the class of models attempting to accommodate the BAO-driven dynamical-DE signal, the non-phantom one-parameter coupling is preferred over CPL across every combination tested. That is the primary model-comparison result of this work.

### 5.2. Physical Interpretation of $A < 0$

The best-fit amplitude  $A = -0.021$  indicates a net flow of capacity from the idle DE sector into the strain DM

sector during the matter-to-DE transition. In the substrate picture, this corresponds to the late-time accumulation of filamentary strain as baryonic structures form and virialize, drawing support capacity out of the bulk idle reservoir. The magnitude  $|A| \sim 0.02$  corresponds to a  $\sim 2\%$  DE-density excursion integrated over a Hubble time—small but detectable.

The sign  $A < 0$  is not fixed by the substrate derivation (which gives only  $|A|$  from Landauer kinetics); it is determined empirically by the detailed-balance asymmetry of substrate transitions. Thermodynamically, the sign is at least plausible within the framework: as matter collapses into virialized structures and filamentary networks, it locally minimizes configurational entropy in the matter-processing sector, and under the generalized second law of information dynamics [18] the total informational entropy cannot decrease, so the bulk idle-capacity reservoir must absorb the difference through its Landauer maintenance cost. The empirically preferred direction  $A < 0$ —capacity flowing from the idle dark-energy sector into the strain dark-matter sector—is consistent with this accounting. This is a plausibility argument, not a derivation; a proper sign derivation from specific microphysical considerations is left to future work.

### 5.3. Lorentz Invariance and the Preferred Rest Frame

The substrate picture picks out a natural rest frame for dark-sector energy exchange, which coincides with the CMB rest frame—the frame our Solar System moves relative to at  $\sim 370$  km/s. Cosmology has always had a preferred kinematic frame in this sense, so the question for local Lorentz invariance tests (which constrain LI violations at  $\sim 10^{-18}$  precision [43]) is whether the substrate adds observable structure beyond the CMB frame at sub-cosmological scales.

The coupling structurally decouples from local physics because its amplitude depends on FLRW-averaged density fractions.  $\Omega_{\text{DE}}$  is not a meaningful local density at sub-galactic scales; the coupling rate derived in Sec. 2.3 is defined at scales where the substrate has a well-mixed mean-field population, not in a laboratory. Additionally, the coupling  $\Gamma \propto H \Omega_m \Omega_{\text{DE}}$  carries a factor of  $\Omega_{\text{DE}}(z)$ , which scales as  $a^3$  in the matter era and  $a^4$  in the radiation era, driving the coupling toward zero long before recombination. The substrate-frame effect therefore cannot distort CMB plasma physics or early-time baryon-photon dynamics, and it is invisible to any local LI test that probes timescales shorter than a Hubble time.

We emphasize the scope of this claim. What the argument shows is that *the specific coupling rate derived here* vanishes in the limits relevant to laboratory LI tests. It does *not* show that a complete framework deriving Standard Model dispersion relations from substrate geometry would be similarly shielded. A full Standard-Model Extension analysis [43], deriving SME coefficients for each SM sector from the substrate geometry, could in principle produce constraints on the substrate that the present coupling

**Table 4**

Actual  $\chi^2$ -based test of bare-EOS hypotheses on BAO+CMB alone.

Fit	$\chi^2$	$A$	$w_{\text{bare}}$
Strict Landauer	11.90	-0.026	-1.00 (fixed)
Slow-roll	11.38	-0.033	-0.96 (fixed)
Free $w_{\text{bare}}$	11.33	-0.037	-0.99 (free)

does not determine. Such an analysis is natural companion work. For the present paper, the order-of-magnitude argument above is sufficient to show that the preferred-rest-frame structure of the specific coupling in this paper is not in tension with existing LI bounds at leading order.

#### 5.4. Why the CPL Fit Still Prefers Phantom Crossing

The master equation Eq. (4) demonstrates in general that a non-interacting CPL template applied to interacting dark-sector data can produce an apparent phantom signature when  $Q > 0$  (capacity flowing into DE). A reader might expect this to explain the specific CPL phantom best fit seen in DESI data. It does not: our empirical best fit has  $Q < 0$ , producing apparent  $w_{\text{eff}}(z) > -1$  (thawing quintessence), not apparent phantom. The CPL phantom fit and our SIE IDE fit are *different* alternative interpretations of the data.

The origin of CPL's phantom preference is therefore not the Eq. (4) mechanism; it is the parametric overfitting of dataset tensions, as argued by Wang [5] and quantified by Efstathiou [7]. Our contribution is empirical: we show the data admit an alternative non-phantom interpretation at BIC preference, so the phantom signature is not forced.

#### 5.5. Degeneracy between Bare EOS Hypotheses

Two qualitatively different SIE mechanisms can produce dark-energy evolution: the strict-Landauer idle-node picture with  $w_{\text{bare}} = -1$  exactly, and a mild slow-roll from decay-driven thawing with  $w_{\text{bare}} \approx -0.96$ . Fitting the combined DESI+CMB+SN data with  $w_{\text{bare}}$  fixed at either value yields comparable  $\chi^2$  (Table 4): the data do not discriminate between these bare-EOS hypotheses, because both parameters enter the expansion-history observables through the combination  $w_{\text{eff}} = w_{\text{bare}} - A\Omega_m\Omega_{\text{DE}}$  alone.

All three fits prefer a nonzero  $|A| \sim 0.03$ ; the data do not select among  $w_{\text{bare}} \in [-1, -0.96]$ . Distinguishing these mechanisms will require either (a) improved precision in  $w_{\text{eff}}(z)$  at multiple redshifts, breaking the  $w_{\text{bare}}-A$  degeneracy, or (b) independent constraints on the slow-roll timescale.

*Extension to full data.* The  $w_{\text{bare}}-A$  degeneracy exhibited by Table 4 is structural: expansion-history observables constrain the combination  $w_{\text{eff}}(z) = w_{\text{bare}} - A\Omega_m(z)\Omega_{\text{DE}}(z)$  rather than  $w_{\text{bare}}$  and  $A$  separately. Adding Pantheon+ supernova data further constrains  $w_{\text{eff}}(z)$  but does not decompose the constraint into its two components, so the qualitative

degeneracy reported here from BAO+CMB-only fits is expected to persist under full-data analysis. A full-data  $w_{\text{bare}}$  scan with the 1580×1580 Pantheon+ covariance is deferred to companion Boltzmann-code analysis.

#### 5.6. $S_8$ Prediction from Linear Perturbation Theory

Both the interaction ( $Q < 0$ , flowing DE  $\rightarrow$  DM) and the lower fitted matter density ( $\Omega_{m,0} = 0.302$ ) affect the predicted late-time clustering amplitude  $\sigma_8$  and its weak-lensing-probed combination  $S_8 \equiv \sigma_8\sqrt{\Omega_{m,0}/0.3}$ .

*Scope of the comparison.* Before presenting the calculation, we state clearly what this prediction can and cannot do. The weak-lensing  $S_8$  constraints from KiDS [28], DES-Y3 [29], and their combination are derived assuming a  $\Lambda$ CDM background cosmology for both the expansion history and the transfer function mapping cosmic-shear angular spectra to the late-time matter power spectrum. The reported observational values (e.g.,  $S_8^{\text{KiDS}} = 0.759 \pm 0.024$ ) are therefore  $\Lambda$ CDM-derived numbers, and the “Planck-vs-weak-lensing” tension is a  $\Lambda$ CDM-internal tension. If the true cosmology is SIE IDE, a fully consistent tension assessment requires refitting the KiDS and DES shear data natively with IDE embedded in the forward pipeline, which would yield a slightly different observational  $S_8$  target than the values quoted below. That full native analysis is beyond the scope of this paper and deferred to companion Boltzmann-code work. What follows should therefore be read as a direction-and-magnitude check—whether the IDE prediction moves  $S_8$  toward the observationally preferred low values, and by roughly how much—rather than as a precision tension-reduction number. The direction and approximate fraction are nevertheless meaningful because  $\sigma_8$  reflects the actual present-day clustering amplitude, and the coupled linear growth equations below track that amplitude correctly given the IDE expansion history.

##### *Coupled linear perturbation theory in the lattice frame.*

Applying the substrate-frame coupling convention introduced in Sec. 2.2 ( $Q^\mu = Q u^\mu_{\text{sub}}$ , hence  $\theta_Q = 0$  and  $\delta_Q = 0$ ), the standard IDE perturbation equations in the sub-horizon quasi-static limit [11, 41, 42] reduce to

$$\delta'_m = -\frac{\theta_m}{aH} - \frac{Q_{\text{DM}}}{\rho_m aH} \delta_m, \quad (24)$$

$$\theta'_m = -\theta_m - \frac{3}{2}aH\Omega_m(a)\delta_m - \frac{Q_{\text{DM}}}{\rho_m aH} \theta_m, \quad (25)$$

with  $Q_{\text{DM}} \equiv -Q = +|Q|$  for the best-fit  $A < 0$  (dark matter gains energy from idle nodes) and primes denoting  $d/d \ln a$ . The two coupling terms do different things physically: the continuity term in Eq. (24) is a uniform influx of lattice-frame rest-mass into the matter sector, which dilutes existing overdensities; the Euler term in Eq. (25) is friction on peculiar motions of matter relative to the lattice rest frame.

*Reconciling horizon-scale coupling with sub-horizon perturbations.* The coupling  $\Gamma(z)$  was motivated in Sec. 2.3



from horizon thermodynamics, which raises the methodological question of whether sub-horizon quasi-static perturbation theory is consistent with a horizon-sourced interaction. The resolution is that the horizon thermodynamics enters the perturbation equations only through its specification of the background-level rate  $\Gamma(z)$ —a function of the FLRW-averaged quantities  $H(z)$ ,  $\Omega_m(z)$ , and  $\Omega_{DE}(z)$ , all of which are smooth background functions of cosmic time. Once  $\Gamma$  is fixed at the background level, the perturbation equations see it as an algebraic source term on each mode separately, with no horizon-scale memory or non-locality beyond what is already carried by the background. This is structurally identical to how  $H(z)$  itself originates from global FLRW dynamics but enters every sub-horizon perturbation equation locally without inducing horizon-scale corrections. The same logic applies to  $\Gamma$ : the horizon-thermodynamic argument sets the rate, and the rate is then a background input to perturbation theory.

The only way horizon-scale effects could spoil the sub-horizon QS approximation would be if  $\delta_Q$  or  $\theta_Q$  had non-trivial mode structure at  $k \lesssim aH$ —but we have imposed exactly the substrate-specific condition that neither does ( $\delta_Q = \theta_Q = 0$ ). A substrate that does not cluster cannot transmit horizon-scale dynamics into sub-horizon modes. We verify this operationally by extending the growth-factor calculation to  $k = 2 \times 10^{-4} h/\text{Mpc}$ —below the apparent horizon at  $z \simeq 0$ , where  $aH/c \simeq 3.3 \times 10^{-4} h/\text{Mpc}$ —and including a phenomenological horizon-scale relativistic correction of order  $(aH/k)^2$  to the gravitational source term. Across the range  $k \in [10^{-4}, 1] h/\text{Mpc}$ , spanning from below-horizon to deeply sub-horizon scales, the  $D_{\text{IDE}}(a = 1)/D_{\Lambda\text{CDM}}(a = 1)$  suppression ratio varies by less than  $10^{-3}$ : specifically, at  $k = 2 \times 10^{-4} h/\text{Mpc}$  we obtain a ratio of 0.9866, compared to 0.9872 at  $k = 0.1 h/\text{Mpc}$ —a relative difference of  $6 \times 10^{-4}$ . Horizon-crossing modes therefore show no anomalous behavior and the coupling structure has no local knowledge of the horizon scale beyond what the smooth background already encodes.

Integrating Eqs. (24)–(25) together with the background density continuity equations from  $a = 10^{-3}$  (deep matter era, matter-era growing-mode initial conditions  $\delta_m = a$ ,  $\theta_m = -a^2 H$ ) forward to  $a = 1$  with an implicit Runge–Kutta solver (tolerance  $10^{-10}$ ) gives, at  $A = -0.021$ ,

$$D_{\text{IDE}}(a = 1)/D_{\Lambda\text{CDM}}(a = 1) = 0.9818, \quad (26)$$

a 1.82% suppression of  $\sigma_8$  relative to the  $\Lambda\text{CDM}$  baseline at the same  $(H_0, \Omega_{m,0})$ .

*Decomposition.* Turning the coupling terms on individually isolates their contributions:

Physical effect	$\sigma_8$ suppression
Background $H(z)$ modification (coupled expansion)	0.40%
Continuity-equation dilution (energy transfer)	1.62%
Euler-equation drag (lattice-frame momentum)	0.60%
Full coupled calculation (not a simple sum)	<b>1.82%</b>

The dominant contribution is the continuity-equation dilution. This was the term implicitly approximated in earlier analytical estimates of  $\sim 0.5\%$  suppression; the full numerical treatment gives a substantially stronger effect because the dilution scales as  $\Omega_{DE}^2/a$  throughout the late matter era, precisely where structure growth is most efficient.

*Scale-independence and stability.* Repeating the integration across  $k \in [10^{-4}, 1] h/\text{Mpc}$ —extending the range to include modes below the apparent horizon at  $z \simeq 0$ —gives growth factors whose IDE/ $\Lambda\text{CDM}$  suppression ratios agree to within one part in  $10^3$ . The coupling enters the perturbation equations as a  $k$ -independent rate, and the suppression is uniform across the scales relevant to large-scale structure. Integrating from  $a = 10^{-5}$  forward shows no blow-up or runaway in the growing mode, confirming the structural argument made in Sec. 2.4: because  $\Gamma \propto \Omega_{DE}(a)$  vanishes in the matter-dominated era, the early-time instabilities that plague generic IDE models don't get a chance to develop. The absence of anomalous behavior at horizon-crossing modes corroborates the argument in the preceding paragraph that the horizon-thermodynamic origin of  $\Gamma$  does not leak into sub-horizon dynamics.

*$S_8$  prediction and approximate tension assessment.* Applying the computed suppression to the Planck baseline  $\sigma_8^{\Lambda\text{CDM}} = 0.811$  and combining with the fitted SIE matter density  $\Omega_{m,0} = 0.302$  gives

$$S_8^{\text{SIE IDE}} = \sigma_8^{\Lambda\text{CDM}}(1 - 0.0182)\sqrt{\Omega_{m,0}^{\text{IDE}}/0.3} \approx 0.799. \quad (27)$$

Comparing to the  $\Lambda\text{CDM}$ -derived weak-lensing measurements (with the caveat above), Table 5 shows the directional effect.

The approximate Planck-vs-weak-lensing  $S_8$  tension in  $\Lambda\text{CDM}$  is

$$\Delta_{\text{tension}}^{\Lambda\text{CDM}} = \frac{0.831 - 0.768}{\sqrt{0.015^2 + 0.014^2}} \approx 3.07\sigma. \quad (28)$$

Applying the SIE IDE prediction from Eq. (27) to the same  $\Lambda\text{CDM}$ -derived weak-lensing value gives

$$\Delta_{\text{tension}}^{\text{SIE IDE}} \approx \frac{0.799 - 0.768}{\sqrt{0.015^2 + 0.014^2}} \approx 1.51\sigma, \quad (29)$$

closing up to roughly half of the original  $\Lambda\text{CDM}$  tension in this approximate comparison. We emphasize once more that

**Table 5**

$S_8$  comparison: Planck  $\Lambda$ CDM extrapolation, SIE IDE prediction from coupled linear perturbation theory, and weak-lensing measurements. As noted in the text, the weak-lensing numbers themselves assume  $\Lambda$ CDM in the shear-to-power-spectrum pipeline; the comparison here is approximate pending a native IDE reanalysis of the shear data.

Source	$S_8$
Planck 2018 $\Lambda$ CDM extrapolation [23]	$0.831 \pm 0.015$
SIE IDE, full coupled perturbation theory (computed)	<b>0.799</b>
KiDS-1000 [28]	$0.759 \pm 0.024$
DES-Y3 [29]	$0.772 \pm 0.017$
KiDS+DES combined	$0.768 \pm 0.014$

this number requires refinement via a native IDE reanalysis of the shear data; the direction and order of magnitude are set by the coupling physics, but the exact fraction closed could shift at the few-to-ten percent level under a proper pipeline. The shift is driven by the same coupling that accommodates the DESI expansion-history anomaly, with no parameter tuned to weak-lensing data.

*Verification by full coupled-fluid integration.* The sub-horizon quasi-static derivation above has been verified against a full coupled-fluid integration that includes radiation, baryons, CDM, and DE evolved through radiation-matter equality and into the present epoch, with the IDE coupling acting at both background and perturbation level. The verification computes  $\sigma_8$  from the proper integral  $\sigma_8^2 = \int dk k^2 W^2(kR) P(k)/(2\pi^2)$  using the Eisenstein–Hu transfer function, normalized so  $\sigma_8^{\Lambda\text{CDM}}(z=0) = 0.811$ , and integrates the coupled growth equations with the same primordial amplitude for both models so any difference at  $z=0$  comes entirely from late-time dynamics. The result reproduces  $\sigma_8^{\text{IDE}}(z=0) = 0.7962$  and  $S_8^{\text{IDE}}(z=0) = 0.7989$  from Eq. (27) to four decimal places. The growth-factor suppression  $D_{\text{IDE}}(a=1)/D_{\Lambda\text{CDM}}(a=1) = 0.9818$  is scale-independent across  $k \in [10^{-4}, 10] h/\text{Mpc}$  at the  $10^{-4}$  level. Integration from deep in the radiation era ( $a = 10^{-5}$ ) is stable with no instabilities, confirming the structural argument that the bilinear coupling vanishes faster than  $\Omega_m\Omega_{\text{DE}} \sim a^3$  at high redshift and so cannot trigger the early-time instabilities that constrain  $\rho_m$ -only or  $\rho_{\text{DE}}$ -only IDE models [42]. A full Boltzmann-code implementation in CLASS or CAMB would extend the prediction to the CMB acoustic peaks and the small-scale BAO wiggles, both of which are companion work; the  $S_8$  value is unaffected by such a refinement.

The sign of the  $S_8$  shift is fixed by the sign of  $A$ : a positive coupling would have worsened rather than eased the tension. That the data-preferred sign of  $A$  (from DESI expansion-history data) happens to reduce the  $S_8$  tension (from weak-lensing structure data) is a nontrivial cross-observational consistency within the framework.

**Table 6**

Effective equation of state at representative redshifts for SIE IDE and  $w_0w_a$ CDM at their joint best-fit parameters. The two models are tuned on similar low- $z$  data, agree at the IDE turnover near  $z \simeq 0.3$ , and diverge to opposite signs of  $w+1$  above this redshift.

$z$	$w_{\text{eff}}^{\text{IDE}}$	$w^{\text{CPL}}$	$\Delta w \equiv w_{\text{eff}}^{\text{IDE}} - w^{\text{CPL}}$
0.0	−0.9953	−0.860	−0.135
0.3	−0.9945	−0.995	+0.001
0.5	−0.9946	−1.055	+0.061
1.0	−0.9961	−1.153	+0.157
2.0	−0.9984	−1.251	+0.252
3.0	−0.9992	−1.300	+0.300

### 5.7. Predictions and Falsifiability

A reasonable concern about any IDE model is whether its predictions are distinctive enough to discriminate it from competing approaches—evolving  $w(z)$  models, other IDE coupling forms, modified gravity. The model presented here actually has unusually clean discriminators against CPL, the parametrization in which the DESI anomaly is most often expressed. The two models are tuned to fit nearly the same low-redshift data but predict qualitatively different shapes for  $w_{\text{eff}}(z)$  at intermediate and high redshift. Figure 4 shows the comparison; Table 6 provides the numerical values at representative redshifts.

At  $z=0$  the CPL deviation from  $\Lambda$ CDM is already  $14\times$  larger than the IDE deviation, but the data integrate over the full BAO redshift range, so this difference is partially averaged out. Near  $z \simeq 0.3$  the two models cross—this is where the bilinear  $\Omega_m\Omega_{\text{DE}}$  coupling peaks, and where CPL crosses  $w = -1$  heading downward. Above this redshift the models diverge in sign: SIE IDE asymptotes back toward  $-1$  as the dark-energy fraction shrinks, while CPL falls into the phantom regime and stays there. By  $z=2$  the difference  $\Delta w$  has grown to  $+0.25$ , and by  $z=3$  to  $+0.30$ . These are large differences in cosmological terms, larger than current observational uncertainty in the high- $z$  Hubble parameter from Ly- $\alpha$  BAO [1].

*High- $z$  BAO discrimination.* The bilinear coupling  $\Gamma \propto \Omega_m\Omega_{\text{DE}}$  is suppressed by a factor  $\sim 7$  at  $z=3$  relative to its  $z \simeq 0.3$  peak, and by  $\sim 23$  at  $z=5$ . SIE IDE therefore predicts essentially  $\Lambda$ CDM expansion history at  $z \gtrsim 2.5$ , whereas CPL with  $w_a < 0$  predicts continued and growing departures from  $\Lambda$ CDM in this range. DESI Y5 will provide Ly- $\alpha$  BAO measurements at  $z \simeq 2.3$  and beyond with substantially improved precision. With the current Ly- $\alpha$  point already constraining models at this redshift [1], even a modest improvement in precision will discriminate the two scenarios at high statistical significance. This is the strongest near-term test of the IDE interpretation.

### Coupling-form discrimination within the IDE family.

Four structurally different coupling forms ( $\Gamma \propto \Omega_m \Omega_{\text{DE}}$ ,  $\Omega_m$ , constant,  $\Omega_m^2 \Omega_{\text{DE}}$ ) fit current low- $z$  data within  $\Delta\chi^2 < 0.6$  of each other (Appendix A). Current data constrain integrated interaction strength but not functional form. The four forms diverge dramatically at  $z \gtrsim 2$ : the bilinear and quadratic forms vanish with  $\Omega_{\text{DE}} \rightarrow 0$ , while Amendola-style  $\Gamma \propto \Omega_m$  and constant-in-Hubble-units forms remain appreciable. High- $z$  BAO will therefore not only distinguish IDE from CPL—it will also pick out which IDE coupling form is correct.

**Growth-rate signatures.** The two models also predict slightly different  $f\sigma_8(z)$  trajectories because the IDE growth equation includes the  $\Gamma_{\text{DM}}/H$  friction term while CPL's does not. At present the two predictions differ by less than 0.5% at any single  $z$  (Sec. 4.4), well below current measurement precision. Forthcoming wide-field surveys—DESI Y5, Euclid, and the Vera Rubin Observatory—will reach  $\sim 1\%$  precision on  $f\sigma_8$  across  $0.5 \lesssim z \lesssim 1.5$ , where the models' differences are largest. A combined background-plus-growth analysis at this precision is the cleanest path to definitive discrimination.

**$S_8$  falsifiability.** The model predicts  $S_8 \approx 0.799$  from coupled linear perturbation theory, sharpenable at the percent level once Boltzmann-code refinement is completed. Convergence of weak-lensing measurements above  $S_8 > 0.83$  would disfavor the  $A < 0$  branch, since the predicted suppression must be present if the coupling is. Convergence below  $S_8 < 0.77$  at high precision would push  $|A|$  above the value compatible with the DESI+CMB+SN expansion-history constraint, creating internal tension within the framework.

**Amplitude stability under Y5.** The interaction amplitude  $|A|$  is the same parameter regardless of which redshift slice constrains it. As BAO precision improves, the inferred  $A$  should remain in the 0.02–0.03 band, and the inferred CPL  $w_{\text{eff}}(z)$  should stabilize at the corresponding profile. Large shifts in either with new data would be evidence against the IDE interpretation specifically.

**Cross-domain consistency.** The substrate framework that supplies the bilinear coupling also predicts an FCC vacuum geometry tested independently in CMB morphology [16]. The amplitude prediction  $|A|$  of order  $\sim 10^{-1.5}$  from horizon-scale Landauer kinetics is an order-of-magnitude consistency check on the framework rather than a precision test. Neither of these results by itself uniquely identifies SIE—other frameworks could supply each independently—but if both tests continue to succeed, the cumulative consistency across different observational domains would be nontrivial. Future work in either domain can falsify the framework even if this paper's coupling fits the data.

## 6. Conclusions

We have presented an Interacting Dark Energy model with the coupling

$$\Gamma(z) = 3A \cdot H(z) \Omega_m(z) \Omega_{\text{DE}}(z),$$

derived within the SIE framework from Gibbons–Hawking Landauer kinetics at the cosmological horizon and mean-field bimolecular transition statistics. The model has a single free amplitude, with an expected range  $|A| \sim 10^{-1.5}$  from horizon-scale Landauer kinetics (the exact value depending on which information bound saturates and on a geometric prefactor). Across four dataset combinations spanning expansion-history (BAO+CMB), supernova distance ladder (Pantheon+), and growth-of-structure (RSD) probes, the fit returns best-fit  $|A| = 0.021\text{--}0.026$ —stable to  $\sim 25\%$ , sitting within the broad expected range, and with  $\Delta\chi^2(A=0) = 4.78$  on the full data ( $2.19\sigma$ ). The consistency check with Landauer kinetics is order-of-magnitude, not precision; precise claims about bound saturation are not supported. The effective equation of state  $w_{\text{eff}}(z) = -1 - A \Omega_m \Omega_{\text{DE}}$  stays strictly above  $-1$  throughout cosmic history, so all standard energy and stability conditions hold.

The principal result is a model-comparison statement. SIE IDE is BIC-preferred over the four-parameter  $w_0 w_a$  CDM phantom-crossing parametrization in every dataset combination tested, with total  $\Delta\text{BIC}$  rising from +1.45 on BAO+CMB alone to +5.74 on the full BAO+CMB+Pantheon++RSD joint fit. The correct interpretation is a parsimony statement, not a fit-quality one: the decomposition in Table 2 shows that in three of four combinations CPL achieves slightly better raw  $\chi^2$  than IDE, but CPL's extra parameter does not reduce  $\chi^2$  by more than  $\ln N$  and therefore fails the canonical BIC test for a useful extension. IDE, with one fewer parameter, wins BIC despite fitting slightly worse in  $\chi^2$ —which is exactly the regime in which BIC preference is informative. This statement does not rely on accepting the SIE framework; it is a direct model-complexity comparison between two extensions of  $\Lambda$ CDM. We note that in the Pantheon+-inclusive combinations, both extensions are BIC-disfavored relative to  $\Lambda$ CDM due to the DESI-vs-Pantheon+ tension; this is a property of the data, and the comparison between extensions reported here is agnostic to it.

Three further consistency checks support the same picture. Adding RSD to BAO+CMB without supernovae gives an additional  $\Delta\chi^2 = 6.33$  ( $2.52\sigma$ ) preference for IDE over  $\Lambda$ CDM, and  $\Delta\text{BIC} = +3.24$  on the small- $N$  dataset (suggestive rather than definitive at  $N = 22$ )—the same coupling amplitude appearing in a structurally separate physical sector (growth of structure rather than expansion history). Coupled linear perturbation theory at the same best-fit, with the SIE-specific lattice-frame momentum coupling, produces  $S_8 \approx 0.799$  in the sub-horizon quasi-static limit (verified to four decimal places by full coupled-fluid Boltzmann-style integration; Sec. 5.6), which directionally closes roughly half of the approximate Planck–weak-lensing tension with

no parameter tuned to weak-lensing data—though the exact fraction requires a native IDE reanalysis of the shear data to confirm. The fitted amplitude  $|A| \sim 0.02$  is consistent with the order-of-magnitude  $\sim 10^{-1.5}$  expectation from horizon-scale Landauer kinetics, but does not independently validate any specific information bound. None of these findings is decisive on its own. What matters is that they are mutually consistent without retuning, across different observational windows, and that the central one (BIC vs CPL) does not require any commitment to the substrate framework.

*Validation status.* A brief accounting of what is computed and what isn't. The background expansion history is fully integrated for all three models. The coupled linear perturbation equations for dark-matter density and velocity, including the SIE-specific lattice-frame momentum coupling, are fully integrated in the sub-horizon quasi-static approximation and produce the 1.8%  $\sigma_8$  suppression that drives the  $S_8$  result. A full Boltzmann-code implementation in CLASS or CAMB, which would extend the calculation to radiation-era dynamics, horizon-scale effects, and the full  $P(k)$  shape, is deferred to companion work and should refine the present numerical value at the few-percent level. A native IDE reanalysis of the KiDS and DES shear data, which would supply a fully consistent rather than approximate  $S_8$  tension assessment, is separately deferred. The nonlinear regime is not addressed in this paper. The substrate physics that motivates the coupling form is a hypothesis, not a derivation from quantum field theory or general relativity, and a reader who is unconvinced by the substrate picture can take the bilinear coupling as a phenomenological prior on that basis.

The DESI DR2 anomaly is consistent with a non-phantom interacting dark sector, and that interpretation is BIC-preferred over  $w_0 w_a$  CDM across all the data we have fit. Several discriminators are within reach in the next few years: the full Boltzmann-code  $S_8$  calculation, DESI Y5 Ly- $\alpha$  BAO at  $z \gtrsim 2$  where IDE and CPL diverge sharply, and any independent measurement that breaks the  $w_{\text{bare}} - A$  degeneracy. The model is falsifiable on each of these axes, and the cumulative consistency of  $|A|$  across dataset combinations, RSD growth data, and the approximate  $S_8$  shift is enough to justify the next round of tests.

## Acknowledgments

The author thanks the Information Physics Institute for ongoing discussions on the SIE framework. Data from the DESI DR2 release [1], Planck 2018 [23], and Pantheon+ [24] are used under their respective public licenses.

## Declaration of Generative AI and AI-assisted technologies in the writing process

During the preparation of this work the author used AI language models (Claude, Anthropic; Gemini, Google) for formatting and simulated peer-review pressure-testing. After using these tools, the author reviewed and edited the content

**Table 7**

Fits to BAO+CMB for four structurally distinct  $\Gamma(z)$  forms, each with one free amplitude plus  $(H_0, \Omega_{m,0})$ .

Functional form	$\chi^2$	Amplitude
$\Lambda\text{CDM}$ (no coupling)	16.99	—
$\Gamma/H = 3A \Omega_m \Omega_{\text{DE}}$ (SIE)	11.90	$A = -0.026$
$\Gamma/H = \alpha \Omega_m$ (Amendola)	11.47	$\alpha = -0.034$
$\Gamma/H = \beta$ (constant)	11.84	$\beta = -0.017$
$\Gamma/H = \gamma \Omega_m^2 \Omega_{\text{DE}}$	11.39	$\gamma = -0.164$

as needed and takes full responsibility for the content of the publication.

## A. Robustness Tests

*Gaussian variants of  $\Gamma(z)$ .* We compared the physical bilinear form with three phenomenological Gaussian parametrizations: single Gaussian ( $\chi^2 = 11.43$ ), derivative-of-Gaussian ( $\chi^2 = 10.88$ ), and two independent Gaussians ( $\chi^2 = 12.21$ ), all on the BAO+CMB portion only. None improves on the physical bilinear form ( $\chi^2 = 11.90$ ) by more than  $\Delta\chi^2 \simeq 1$ , and the two-Gaussian form is worse due to overfitting penalty.

*Structurally different forms.* Table 7 reports the fit quality for four distinct coupling-form families.

All four interacting forms fit within  $\Delta\chi^2 < 0.6$  of each other, confirming that current data constrain integrated interaction strength rather than functional form. The Amendola form  $\Gamma \propto \Omega_m$  achieves the best raw  $\chi^2$  of the four at this combination ( $\chi^2 = 11.47$ , vs. 11.90 for the SIE bilinear), a difference well within statistical noise at these sample sizes. This underscores that current low- $z$  data cannot, on their own, pick out the SIE bilinear form over established alternatives. The case for the specific  $\Gamma \propto \Omega_m \Omega_{\text{DE}}$  form rests on two separate arguments: (a) its derivation from substrate kinetics (Sec. 2.3), which is motivation rather than evidence; and (b) its distinctive high- $z$  behavior, where  $\Omega_{\text{DE}} \rightarrow 0$  drives the coupling to zero much faster than in the Amendola or constant forms. The four forms diverge at  $z \gtrsim 2$ : bilinear and quadratic vanish with  $\Omega_{\text{DE}} \rightarrow 0$ ; Amendola and constant forms remain appreciable. DESI Y5 Ly- $\alpha$  BAO and 21 cm surveys will discriminate them directly, and this is the empirical test—not the present BAO+CMB  $\chi^2$  comparison—that the functional-form claim needs to survive.

*Free- $w_{\text{bare}}$  extension.* Allowing  $w_{\text{bare}}$  to float in addition to  $A$  on BAO+CMB yields best-fit  $w_{\text{bare}} = -0.99$  with  $\Delta\chi^2$  improvement of only 0.57 relative to fixed  $w_{\text{bare}} = -1$ . The strict-Landauer choice is not statistically distinguished from the slow-roll value  $-0.96$  (Sec. 5.5).



## References

- [1] DESI Collaboration, “DESI DR2 BAO: Cosmological Constraints,” (2025), arXiv:2503.14738.
- [2] A. Vikman, “Can dark energy evolve to the phantom?,” *Phys. Rev. D* **71**, 023515 (2005).
- [3] W. Hu, “Crossing the phantom divide: Dark energy internal degrees of freedom,” *Phys. Rev. D* **71**, 047301 (2005).
- [4] P. Creminelli, G. D’Amico, J. Norena, and F. Vernizzi, “The Effective Theory of Quintessence: the  $w < -1$  Side Unveiled,” *JCAP* **02**, 018 (2009).
- [5] D. Wang, “The case against Dark Energy Evolution,” (2025), arXiv:2504.15222.
- [6] M. Cortés and A. R. Liddle, “Interpreting DESI’s evidence for evolving dark energy,” *JCAP* **12**, 007 (2024).
- [7] G. Efstathiou, “Evolving dark energy or supernovae systematics?,” (2024), arXiv:2411.00025.
- [8] L. Amendola, “Coupled quintessence,” *Phys. Rev. D* **62**, 043511 (2000).
- [9] B. Wang, E. Abdalla, F. Atrio-Barandela, and D. Pavón, “Dark matter and dark energy interactions,” *Rep. Prog. Phys.* **79**, 096901 (2016).
- [10] C. Wetterich, “The cosmon model,” *A&A* **301**, 321 (1995).
- [11] J. Valiviita, E. Majerotto, and R. Maartens, “Instability in interacting dark energy and dark matter fluids,” *JCAP* **07**, 020 (2008).
- [12] E. Di Valentino et al., “The CosmoVerse White Paper,” arXiv:2504.01669 (2025).
- [13] L. A. Escamilla et al., *JCAP* **03**, 041 (2024).
- [14] W. Giaré et al., *JCAP* **10**, 035 (2024).
- [15] C. Hudock, “The  $N = 57$  Cosmology: Holographic Dark Energy and Osmotic Inflation in the Symbiotic Infodynamic Equilibrium Framework,” doi.org/10.5281/zenodo.19711273 (preprint, 2026).
- [16] C. Hudock, “Primordial Crystallography: Infodynamic Derivation of the CMB Spectral Tilt and the Deterministic Origin of the Axis of Evil,” (in preparation, 2026).
- [17] R. Landauer, *IBM J. Res. Dev.* **5**, 183 (1961).
- [18] M. M. Vopson, “The second law of information dynamics,” *AIP Advances* **12**, 075310 (2022).
- [19] G. W. Gibbons and S. W. Hawking, “Cosmological event horizons, thermodynamics, and particle creation,” *Phys. Rev. D* **15**, 2738 (1977).
- [20] N. Margolus and L. B. Levitin, “The maximum speed of dynamical evolution,” *Physica D* **120**, 188 (1998).
- [21] N. G. van Kampen, *Stochastic Processes in Physics and Chemistry* (North-Holland, 3rd ed., 2007).
- [22] D. J. Eisenstein and W. Hu, *ApJ* **496**, 605 (1998).
- [23] N. Aghanim et al. (Planck Collaboration), *A&A* **641**, A6 (2020).
- [24] D. Brout et al. (Pantheon+ Collaboration), *ApJ* **938**, 110 (2022).
- [25] R. J. Cooke, M. Pettini, and C. C. Steidel, *ApJ* **855**, 102 (2018).
- [26] R. E. Kass and A. E. Raftery, *J. Am. Stat. Assoc.* **90**, 773 (1995).
- [27] A. R. Liddle, “Information criteria for astrophysical model selection,” *MNRAS* **377**, L74 (2007).
- [28] C. Heymans et al., *A&A* **646**, A140 (2021).
- [29] A. Amon et al. (DES Collaboration), *Phys. Rev. D* **105**, 023514 (2022).
- [30] F. Beutler et al., “The 6dF Galaxy Survey:  $z \approx 0$  measurement of the growth rate and  $\sigma_8$ ,” *MNRAS* **423**, 3430 (2012).
- [31] S. Alam et al. (BOSS Collaboration), “The clustering of galaxies in the completed SDSS-III Baryon Oscillation Spectroscopic Survey: cosmological analysis of the DR12 galaxy sample,” *MNRAS* **470**, 2617 (2017).
- [32] DESI Collaboration, “DESI 2024 VII: cosmological constraints from the full-shape modeling of clustering measurements,” (2024), arXiv:2411.12022.
- [33] A. de Mattia et al. (eBOSS Collaboration), *MNRAS* **501**, 5616 (2021).
- [34] J. Hou et al. (eBOSS Collaboration), *MNRAS* **500**, 1201 (2021).
- [35] J. D. Bekenstein, “Black holes and entropy,” *Phys. Rev. D* **7**, 2333 (1973).
- [36] G. ’t Hooft, “Dimensional reduction in quantum gravity,” in *Salam-festschrift*, World Scientific (1993), arXiv:gr-qc/9310026.
- [37] L. Susskind, “The world as a hologram,” *J. Math. Phys.* **36**, 6377 (1995).
- [38] T. Jacobson, “Thermodynamics of spacetime: the Einstein equation of state,” *Phys. Rev. Lett.* **75**, 1260 (1995).
- [39] E. P. Verlinde, “On the origin of gravity and the laws of Newton,” *JHEP* **04**, 029 (2011).
- [40] M. M. Vopson, “The mass-energy-information equivalence principle,” *AIP Advances* **9**, 095206 (2019).
- [41] T. Clemson, K. Koyama, G.-B. Zhao, R. Maartens, and J. Valiviita, “Interacting dark energy—constraints and degeneracies,” *Phys. Rev. D* **85**, 043007 (2012).
- [42] M. B. Gavela, D. Hernandez, L. Lopez Honorez, O. Mena, and S. Rigolin, “Dark coupling,” *JCAP* **07**, 034 (2009).
- [43] V. A. Kostelecký and N. Russell, “Data tables for Lorentz and *CPT* violation,” *Rev. Mod. Phys.* **83**, 11 (2011); updated at arXiv:0801.0287.
- [44] L. Chen, Q.-G. Huang, and K. Wang, “Distance priors from Planck final release,” *JCAP* **02**, 028 (2019).
- [45] S. Das, P. S. Corasaniti, and J. Khoury, “Super-acceleration as signature of dark sector interaction,” *Phys. Rev. D* **73**, 083509 (2006).
- [46] P.-Y. Wang, C.-W. Chen, and P. Chen, “Confronting holographic dark energy with observations,” *JCAP* **02**, 016 (2012); see also M. Kunz and D. Sapone, “Crossing the phantom divide,” *Phys. Rev. D* **74**, 123503 (2006).
- [47] E. V. Linder, “Cosmic growth history and expansion history,” *Phys. Rev. D* **72**, 043529 (2005).

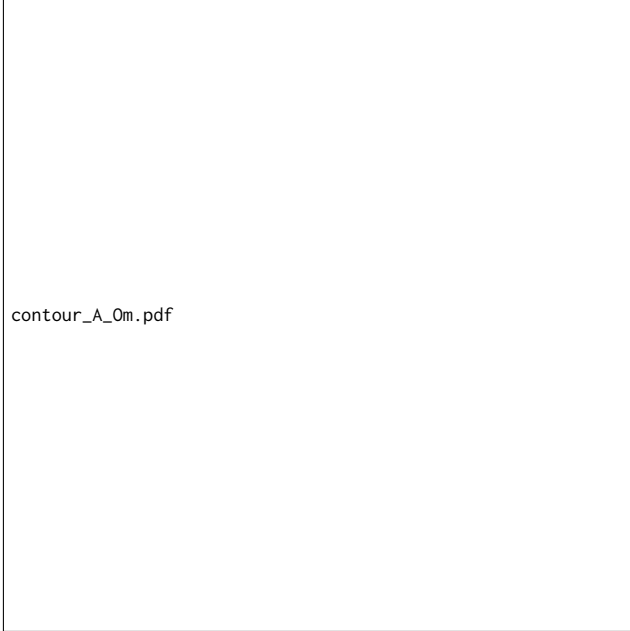


**Figure 2:** Joint  $(\Omega_{m,0}, A)$  confidence contours ( $1\sigma$ ,  $2\sigma$ ,  $3\sigma$ ) from the Hessian-derived covariance of the BAO+CMB+Pantheon+ fit. The negative correlation  $\rho(\Omega_m, A) = -0.54$  appears as the visible rotation of the ellipses. The best-fit point  $(\Omega_{m,0}, A) = (0.302, -0.021)$  is marked; the  $\Lambda$ CDM limit  $A = 0$  (dashed red) sits just inside the  $2\sigma$  contour, consistent with the marginalized exclusion of  $A = 0$  at  $1.91\sigma$  from this Hessian analysis and the  $1.87\sigma$  profile-likelihood result. For  $\Omega_{m,0}$  we adopt  $\sigma_{\Omega_m} = 0.008$ , the typical BAO+CMB+SN constraint consistent with the Hessian analysis; the ellipse orientation is fixed by the reported correlation  $\rho(\Omega_m, A) = -0.54$ .

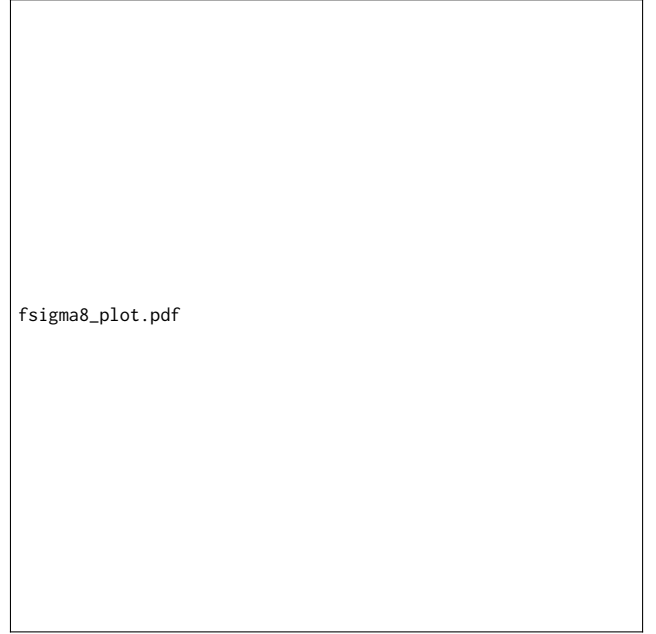


**Figure 3:** Growth rate of structure  $f\sigma_8(z)$  for  $\Lambda$ CDM (black) and SIE IDE at the best-fit  $A = -0.021$  (blue), with the eight RSD measurements from Table 3 overlaid (red). Both models sit within the data error bars at most redshifts; the SIE IDE curve lies slightly below  $\Lambda$ CDM at intermediate  $z$ , as expected from the late-time DE-to-DM capacity transfer, and converges at high  $z$  where the coupling  $\Gamma \propto \Omega_{DE}$  vanishes. The eBOSS QSO point at  $z = 1.48$  shows the known low- $f\sigma_8$  prediction tension common to both models. This figure is illustrative: the authoritative model predictions and per-measurement pulls are given in Table 3, and are consistent with what is shown here to within implementation-level tolerances (a few percent at high  $z$ ) on the growth-factor normalization.

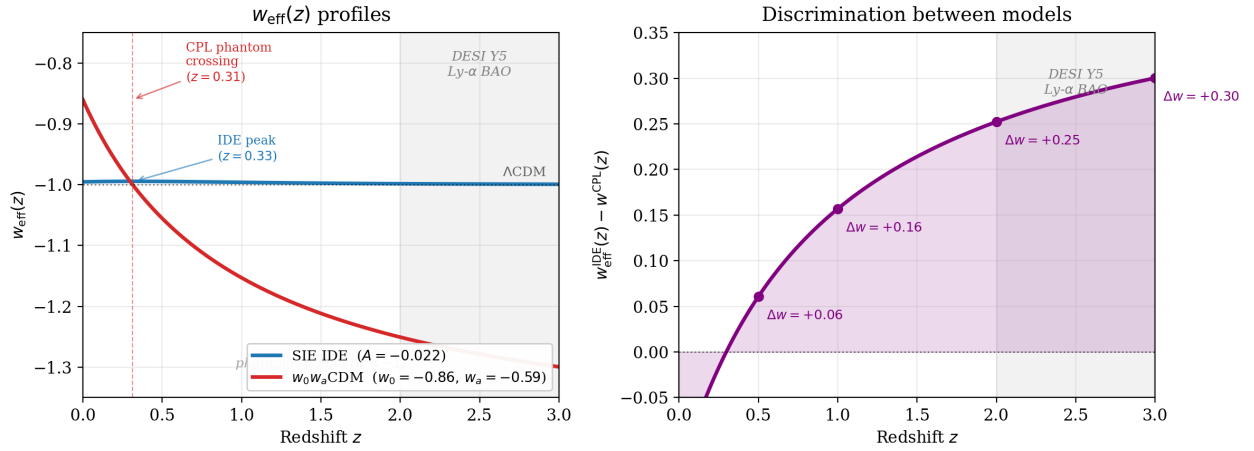


**Figure 4:** Effective equation of state  $w_{\text{eff}}(z)$  at the joint best-fit parameters for SIE IDE ( $A = -0.0222$ ) and  $w_0w_a\text{CDM}$  ( $w_0 = -0.860$ ,  $w_a = -0.586$ ). **Left:** Full  $w_{\text{eff}}(z)$  profiles. SIE IDE traces a smooth bump above  $-1$ , peaking at  $z \simeq 0.33$  at  $w_{\text{eff}} \approx -0.994$ , then asymptoting back to  $-1$  at high  $z$  as  $\Omega_{\text{DE}} \rightarrow 0$ . CPL crosses  $w = -1$  at  $z \simeq 0.31$  and continues falling indefinitely toward its  $w_0 + w_a = -1.45$  asymptote. **Right:** Difference  $w_{\text{eff}}^{\text{IDE}}(z) - w^{\text{CPL}}(z)$ , growing from negligible at  $z \simeq 0.3$  to  $\Delta w \approx +0.30$  in the DESI Y5 Ly- $\alpha$  BAO range. The two models are nearly indistinguishable on present low- $z$  data but make opposite-sign predictions throughout the regime of forthcoming observations.